

The Properties of X-ray Luminous Young Stellar Objects in the NGC 1333 and Serpens Embedded Clusters.

E. Winston^{1,2,10}, S. T. Megeath³, S. J. Wolk², B. Spitzbart², R. Gutermuth^{4,5}, L.E. Allen⁶, J. Hernandez^{7,8}, K. Covey², J. Muzerolle⁹, J. L. Hora², P. C. Myers², G. G. Fazio²

ewinston@astro.ex.ac.uk

ABSTRACT

We present new *Chandra* X-ray data of the NGC 1333 embedded cluster and combine these data with existing *Chandra* data, *Spitzer* photometry and ground based spectroscopy of both the NGC 1333 and Serpens Cloud Core clusters to perform a detailed study of the X-ray properties of two of the nearest embedded clusters to the Sun.

We first present new, deeper observations of NGC 1333 with *Chandra ACIS-I* and combine these with existing *Spitzer* observations of the region. In NGC 1333, a total of 95 cluster members are detected in X-rays, of which 54 were previously identified in the *Spitzer* data. Of the *Spitzer* identified sources, we detected 23% of the Class I protostars, 53% of the Flat Spectrum sources, 52% of the Class II, and 50% of the Transition Disk young stellar objects (YSO). Forty-one

¹School of Physics, University of Exeter, Stocker Road, Exeter, EX4 4QL, U.K.

²Harvard Smithsonian Center for Astrophysics, 60 Garden St., Cambridge MA 02138, USA.

³Ritter Observatory, Dept. of Physics and Astronomy, University of Toledo, 2801 W. Bancroft Ave., Toledo, OH 43606, USA.

⁴Five Colleges Astronomy Department, Smith College, Northampton, MA 01027

⁵Department of Astronomy, University of Massachusetts, Amherst, MA 01003

⁶NOAO, Tucson, AZ, USA.

⁷Centro de Investigaciones de Astronomia, Apdo. Postal 264, Merida 5101-A, Venezuela.

⁸Department of Astronomy, University of Michigan, Ann Arbor, MI 48109.

⁹Space Telescope Science Institute, Baltimore, MD, USA.

¹⁰Visiting Astronomer at the Infrared Telescope Facility, which is operated by the University of Hawaii under Co-operative Agreement no. NCC 5-538 with the National Aeronautics and Space Administration, Science Mission Directorate, Planetary Astronomy Program.

Class III members of the cluster are identified, bringing the total identified YSO population to 178.

The X-ray Luminosity Functions (XLFs) of the NGC 1333 and Serpens clusters are compared to each other and the Orion Nebula Cluster. Based on a comparison of the XLFs of the Serpens and NGC 1333 clusters to the previously published ONC, we obtain a new distance for the Serpens cluster of 360^{+22}_{-13} pc.

Using our previously published spectral types, effective temperatures and bolometric luminosities, we analyze the dependence of the X-ray emission on the measured stellar properties. The X-ray luminosity was found to depend on the calculated bolometric luminosity as in previous studies of other clusters. We examine the dependence of L_X on stellar surface area and effective temperature, and find that L_X depends primarily on the stellar surface area. In the NGC 1333 cluster, the Class III sources have a somewhat higher X-ray luminosity for a given surface area. We also find evidence in NGC 1333 for a jump in the X-ray luminosity between spectral types of M0 and K7, we speculate that this may result from the presence of radiative zones in the K-stars.

The gas column density vs. extinction in the NGC 1333 parental molecular cloud was examined using the Hydrogen column density determined from the X-ray absorption to the embedded stars and the K -band extinction measured to those stars. In NGC 1333, we find $N_H = 0.89 \pm 0.13 \times 10^{22} A_K$, this is lower than expected of the standard ISM but similar to that found previously in the Serpens Cloud Core.

Subject headings: infrared: stars — X-rays: stars — stars: pre-main sequence — circumstellar matter

October 26, 2018

1. Introduction

In recent years many studies of young stellar clusters have been undertaken to investigate the emission properties of pre-main sequence stars and protostars in the higher energy X-ray regime (Wolk et al. 2006; Getman et al. 2005; Preibisch & Feigelson 2005). These studies compliment those carried out in the mid-IR, where young stars are identified by the excess emission produced through the reprocessing of stellar radiation by circumstellar material. Optical and near-IR spectroscopic observations of the young stars in these regions

add information on the fundamental properties of the stars, such as effective temperature and luminosity.

Young stellar objects (YSOs) often possess levels of X-ray emission elevated to $L_X \sim 10^4 \times L_{X\odot}$, this elevated emission can be used to distinguish them from field stars (Feigelson & Montmerle 1999; Feigelson & Kriss 1981). In developed, hydrogen burning stars, X-ray activity arises from magnetic fields generated as a result of shear between the core radiative zone and the outer convective zone. The process behind the generation of the highly increased levels of emission in young stellar objects remains uncertain since low mass pre-main sequence stars are often fully convective. Some suggested causes are magnetic disk-locking between the star and disk (Hayashi et al. 1996; Isobe et al. 2003; Romanov et al. 2004), accretion onto the star (Kastner et al. 2002; Favata et al. 2003, 2005), and alternative dynamo models for coronal emission (Küker & Rüdiger 1999; Giampapa et al. 1996).

We present a study of X-ray emitting young stars in the Serpens and NGC 1333 clusters. These two clusters are examples of nearby (<0.5 kpc), low mass regions with high fractions of protostars yet different spatial geometries and frequencies of jets. Both are deeply embedded in their natal clouds. Serpens is the more deeply embedded with extinctions exceeding 40 magnitudes in the visual. IR and submm observations identify at least 38 protostars in the central core region, and more than 130 embedded young stars in total (Testi et al. 1998, 2000; Davis et al. 1999; Hogerheijde et al. 1999; Winston et al. 2007). An age of ≤ 2 Myrs has been found for the cluster (Kaas et al. 2004; Winston et al. 2009), with some evidence for a halo of older sources surrounding the central core (see Winston et al. 2009, for a discussion of the possible age spread.) The Chandra X-ray observations of Serpens have previously been reported by Giardino et al. (2007) and Winston et al. (2007). NGC 1333 contains a high number of embedded protostars, cores and outflows (Knee & Sandell 2000), and while showing a spread in isochronal ages was found to have a median age of 2 Myrs (Winston et al. 2009). The region has previously been observed in X-rays with ROSAT by Preibisch (1997) who identify 16 YSOs. A study by Getman et al. (2002) with *Chandra* associated 95 detections with cluster members and found no difference in X-ray luminosity between Classical T-Tauri stars (CTTS) and weak line T-Tauri stars (WTTS). Preibisch (2003) observed NGC 1333 using XMM, detecting 86 sources in the region. Optical and IR surveys to identify the YSOs in the region have been carried out by Aspin et al. (1994), Wilking et al. (2004), Lada et al. (1996), Gutermuth et al. (2008b) and Gutermuth et al. (2009). Over 160 young stars have been identified in the cluster. NGC 1333 does not appear to be centrally condensed though the protostars are observed to trace the underlying gas distribution, whereas the Serpens protostars are located along a filament in the centre of the cluster.

There are four main results in this paper. First, we utilise the elevated X-ray luminosity

to identify YSOs in the NGC 1333 region that do not exhibit IR-emission from a dusty disk (evolutionary Class III) and would otherwise be indistinguishable from field stars using *Spitzer* photometry. Protostars (Class 0/I and Flat Spectrum) and pre-main sequence stars with disks (Class II and Transition Disks) may also show elevated X-ray emission and we identify such objects with detectable X-ray emission.

Second, we use the X-ray data to redetermine the distance to the Serpens cluster. One of the more elusive properties of Young Stellar Clusters (YSCs) is an accurate measure of their distances. The distance underpins luminosity calculations, and therefore the determination of the stellar isochronal ages and masses. The distance to NGC 1333 has recently been measured based on a VERA measurement of maser parallax toward SVS 13 to be at 240 pc, and this is the distance used in this study (Hirota et al. 2008). A method for determining the distance to YSCs based on the comparison of the X-ray luminosity function (XLF) to a ‘universal’ XLF (Feigelson et al. 2005) is applied to the Serpens data to obtain a more accurate distance to the cluster. The most commonly adopted distance to the Serpens Cloud is 260 pc based on an extinction versus distance diagram to ~ 450 stars using Vilnius seven-color photometry (a discussion of the distance is given in Straizys et al. 2003). Other estimates have ranged from 700 pc (Zhang et al. 1988) to 440 pc (Racine 1968; Strom et al. 1974) and 310 pc (de Lara et al. 1991). Here we will attempt to judge the distance via a technique applied to the YSOs in the cluster themselves.

In the third section, we present a detailed study of the combined spectral and X-ray properties of the populations of YSOs as a function of their evolutionary class in the Serpens and NGC 1333 clusters, identified by observations with *Spitzer* and *Chandra* and published by Gutermuth et al. (2008a) and Winston et al. (2007, 2009). *Chandra* has recently examined the X-ray properties of the Orion Nebula Cluster (ONC), in a project known as the *Chandra* Orion Ultra-Deep Project (COUP). Although the Serpens and NGC 1333 samples are much smaller than the COUP survey, the analysis of these two smaller clusters has the advantage of excellent $3.6\text{--}24\ \mu\text{m}$ photometry; observations longward of $4.5\ \mu\text{m}$ are difficult in the centre of the ONC due to the bright infrared emission from the molecular cloud. This photometry allows us to accurately ascertain the evolutionary class of each object, and study the dependence of the X-ray properties on evolutionary state. Further, optical and infrared spectroscopy has been obtained and used to determine the effective temperatures, bolometric luminosities, and stellar surface areas of a number of the YSOs. With these data, we can examine the X-ray flux to bolometric luminosity by evolutionary class, and examine the dependence on surface area and effective temperature in these two clusters.

Finally, we derive the relationship between Hydrogen column density derived from X-ray data and near-infrared extinction. Consistent with our preliminary work, we find that

in these molecular clouds, the hydrogen column density per magnitude of K-band extinction is $\sim 1/3$ that in the diffuse ISM. This may be the result of grain growth and coagulation in cold, dense molecular clouds.

2. Observations and Data Reduction

2.1. *Spitzer* & 2MASS IR Photometry

We have obtained *Spitzer* images of the Serpens and NGC 1333 regions in six wavelength bands: the 3.6, 4.5, 5.8 and 8.0 μm bands of the Infrared Array Camera (IRAC; Fazio et al. (2004)) and the 24 μm and 70 μm bands of the Multi-band Imaging Photometer for *Spitzer* (MIPS; Rieke et al. (2004)). The photometry extracted from these data was supplemented by *J*, *H* and *K_S*-band photometry from the 2MASS point source catalogue (Skrutskie et al. 2006), resulting in data in nine photometric bands spanning 1-70 μm . The observations, image reduction and photometry for the *Spitzer* data have previously been presented by Winston et al. (2007) and Gutermuth et al. (2008b). In Serpens, Winston et al. (2007) identified 117 YSOs with IR-excesses: 22 Class 0/I objects, 16 Flat Spectrum, 62 Class II and 17 Transition Disks (see Winston et al. 2009, on contamination of Transition Disk objects by AGB stars.) In comparison, Gutermuth et al. (2008b) identified 137 YSOs in NGC 1333: 11 candidate Class 0, 26 Class I, 16 Flat Spectrum, 80 Class II and 4 Transition Disks (note that the Flat Spectrum classification was applied to the NGC 1333 catalog by Winston et al. 2009).

2.2. *Chandra* Data Reduction

The X-ray data were taken from the *Chandra* ANCHORS (AN archive of CHandra Observations of Regions of Star formation¹) archive. The Serpens cluster was observed on June 19th 2004, OBSID 4479, with a 88.45 ks exposure time, the field centered on the *J*2000 coordinates: $18^{\text{h}}29^{\text{m}}50^{\text{s}}$, $+01^{\text{d}}15^{\text{m}}30^{\text{s}}$. The Serpens observations have been previously published in Giardino et al. (2007) and Winston et al. (2007). The NGC 1333 data is newly published here, hence we describe the reduction of the NGC 1333 data in detail. NGC 1333 was observed in three epochs: OBSID 6436, a 36.95 ks exposure on July 5th 2006, OBSID 6437, a 40.12 ks exposure on July 11th, 2006, and OBSID 642, a 43.91 ks exposure on July 12th 2000, giving a total exposure time of 120.98 ks. The 2006 fields were centred on

¹<http://cxc.harvard.edu/ANCHORS/>

the *J*2000 coordinates: $03^h29^m02.0^s, +31^d20^m54^s$, with the 2000 field centred on the *J*2000 coordinates: $03^h29^m05.6^s, +31^d19^m19^s$. These three epochs are combined to provide the final source list used in this analysis, with a total of 180 point sources detected in the field. Table 1 lists the identifiers, coordinates and properties of the 180 sources identified in NGC 1333. The table provides the *Chandra* identifier, source locations, the raw and net number counts (net counts are background subtracted and aperture corrected), plasma temperature (kT), hydrogen column density (N_H), absorbed and unabsorbed X-ray flux (F_X), and flaring statistics. The field of view of *Chandra* is $17'$, smaller than that covered by the IR data: thus not all IR-identified cluster members were observed at X-ray wavelengths.

2.2.1. Source Detection

For NGC 1333, the three separate epochs were first combined using the `merge_all` script². This wrapper script uses standard *ciao* tools to create a merged event file. The inputs were the individual event files and the level 1 aspect solution data products. The event files were standard level 2 products with an energy filter of 0.3-8.0 keV and a spatial filter to select CCD chips 0-3 applied. We used obsid 6437 (the latest observation) as the coordinate reference to which the other observations have their coordinates reprojected. With the merged event file we ran a recursive blocking source detection algorithm. In this scheme, we performed two iterations using the *ciao* wavlet based source detection tool, *wavdetect*. The first pass looked at a square region $15' \times 15'$ on each side and centered at the aimpoint with full resolution. The second pass examined a $25' \times 25'$ area including all six ACIS chips with pixels binned by two.

Source and background regions were determined separately for the three datasets. The program *dmcoords* was used to convert the WCS coordinates of the merged events list back to the physical coordinates in the individual observations. From the detected source positions, we create elliptical source extraction regions for the 3 individual datasets. For each source, the parameters of the ellipse are the size of the semimajor and semiminor axis as well as the orientation angle of the ellipse, ρ . Allen, Jerius, & Gaetz (2004) have produced a parameterization of the axial description of the Chandra point spread function by using observed data. The ellipse semimajor and semiminor axes for a given encircled energy fraction (ECF) and energy can be interpolated from the lookup table as a function of azimuth angle, ϕ , measured in degrees, and off-axis angle, θ .³ The size of the ellipse axis

²Chandra contributed software - <http://cxc.harvard.edu/ciao/download/contrib.html>

³A lookup table of the parameterization is available at: <http://cxc.harvard.edu/cal/Hrma/psf/ECF/hrmaD1996-12-20hrci>.

are determined by a linear interpolation. The table value for the off-axis angle nearest the source, at 95% ECF and 1.0 keV is used. The interpolation is then between the nearest adjacent azimuth angles. Due to the coarse grid of this calibration parameterization, it is impractical to interpolate the proper ellipse angle, ρ . Therefore, we used the CIAO tool *mkpsf* to obtain images of the PSF at a finer grid of off-axis and azimuthal angles around the ACIS array. We fit ellipses at each location, and derived a general empirical formula: $\rho = (\phi \times 0.47 + 146.6 - \text{ROLL} + 360) \bmod 180$. A centroid algorithm is then applied to the source ellipse to balance the distribution of photons within the ellipse in the actual dataset. Background regions were defined as similar elliptical annuli, centered on the source position. The outer semimajor and semiminor axes were 6 times the size of the source ellipse and the inner axes 3 times the source. Finally a check was done to identify nearby or overlapping sources. These sources are removed from the source extraction area with exclusion regions of ellipses 3 times the original source size. Finally, *psextract* was run to create appropriate files for spectral fitting. *Psextract* follows the standard CIAO 3.4 threads⁴. First, *dmextract* is used to create the source and background spectra in Pulse Height Amplitude (PHA) space. Then, *dmstat* lists the chip location of the source and background regions and *acis-fef-lookup* uses this information to identify the appropriate spectral calibration files (FEFs). Then *mkrmf* applies the FEF to create the source and background Response Matrix Function (RMF). These files are used by *Sherpa* to convert PHA channels to energy. In most cases, because the source and background regions have the same average detector coordinates, the two files are the same. Next, *asphist* is used to create the aspect histogram, which is a binned representation of aspect motion during the observation. This is then applied by *mkarf* to create an appropriate Ancillary Response Function (ARF). The ARF contains the combined telescope/filter/detector areas (“effective area”) and the quantum efficiency (QE) as a function of energy averaged over time.

2.2.2. Spectral Analysis

We used the CXC SHERPA program to generate spectral fits and solve simultaneously for the absorbing column of hydrogen, N_H , and the temperature of the thermal plasma, kT . The results incorporate simultaneous fits of the three observations by defining each spectrum independently and fitting with the same model for a result which minimizes the combined residuals. We fit the unbinned spectra to a one temperature Raymond-Smith model. In the case of NGC 1333, the temporal spread in the data means that the temperature and flux of the sources could change between epochs; the reported fits are ef-

⁴<http://cxc.harvard.edu/ciao3.4/threads/ispec.html>

fectively an average of the data from the epochs. We used unbinned data fitted using CSTAT statistics and Powell optimization. This combination is more robust in avoiding local minimizations, which binned methods tend toward. This also gives more reliable results in low count sources. This later point was especially important for NGC 1333 in which the observations were thrice divided and hence we would have required about 30 counts in each observation for successful binned fits. Recent work by Siemiginowska (2008; <http://cxc.harvard.edu/sherpa/references/papers/statistics.pdf>) also indicates that unbinned statistics are less biased than the binned form. We used a model background consisting of a constant, power-law, and Gaussian to resemble a typical ACIS background. X-ray fluxes are estimated using *Sherpa's* *eflux* function. We calculate the total integrated energy flux over our standard energy range (0.3-8.0 keV). A flux is returned in units of $\text{ergs}/\text{cm}^2/\text{sec}$. This is repeated using only the kT model component to obtain the unabsorbed flux. The values are scaled up from the 95% encircled energy radius for the final published values.

2.3. Optical & Near-IR Spectroscopy

To undertake a more thorough examination of the X-ray properties of the two young clusters, we obtained spectral observations of members identified by the *Spitzer* and *Chandra* observations (as well as a number of stars surrounding the clusters to search for additional members). The spectral observations of both clusters were obtained using the Hectospec instrument on MMT and the SpeX instrument on IRTF. A full analysis of these data can be found in the companion paper Winston et al. (2009), where a comparison with the IR photometry and evolutionary classifications of the sources is undertaken. Hectospec, on the MMT, provides simultaneous far-red (6000-9000 Å) spectra of up to 300 objects, and was used to observe the less embedded known cluster members and to search for diskless members not detected by Chandra. SpeX on the IRTF provided spectra of known, more deeply embedded Class II and III members, over the *H*, and *K*-bands. A brief summary of the relevant points from the companion paper is provided: In total, spectral types were obtained for 64 young stellar objects (YSOs) in Serpens, with a further 74 in NGC 1333. All of the SpeX sources were known cluster members, while eight (4 in Serpens, 4 in NGC 1333) of the Hectospec sources are possible new diskless young stellar objects that were not detected in the *Chandra* data but show *Li I* absorption, an indicator of stellar youth. We determined spectral types for 60 and 70 previously identified YSOs in Serpens and NGC1333, respectively. Of these members with spectral types, 34 and 59 have *Chandra* X-ray counterparts in Serpens and NGC 1333, respectively.

3. X-ray Characteristics of the NGC 1333 YSOs

3.1. YSO Detection Rates

Previous infrared studies by Gutermuth et al. (2008b) have revealed 137 YSOs with IR-excess emission in the NGC 1333 cluster. The *Chandra* observations of the region identified 180 point sources, of which 95 were matched to an IRAC or 2MASS detection in at least one IR band, with a maximum separation between the *Chandra* and IR positions of $1.12''$. Table 1 lists the coordinates and X-ray properties of the 180 X-ray point sources in the *Chandra* catalogue. Table 2 lists the *Chandra* identifier and coordinates, the infrared coordinates and IR photometry of the 95 X-ray detections with an IR counterpart. The formal uncertainties for each *Spitzer* magnitude are listed; in addition to these uncertainties is an approximately 5% uncertainty in the calibration. The remaining 85 X-ray sources were not detected in any IR band and were randomly distributed across the field of view, and are therefore considered to be background contamination from AGN. In this paper we use the classification scheme used in Winston et al. (2007): Class 0/I sources, with rising spectral energy distributions (SEDs) with $\alpha > 0.3$ where $\alpha = \frac{d\lambda F_\lambda}{d\lambda}$, Flat Spectrum sources with flat SEDs and $-0.3 < \alpha < 0.3$, Class II sources with decreasing SEDs ($\alpha < -0.3$), Transition Disks which show weak infrared excesses at 3-8 μm and are thought to have large holes in their inner disks, and Class III members of the cluster which lack an infrared excess.

Of the remaining 95 X-ray sources with an IR counterpart, 54 were known IR YSOs. The remaining 41 sources exhibited no IR-excess emission and were identified as YSOs solely by their elevated X-ray emission. These sources are Class III diskless members of the cluster, bringing the total number of cluster members to 178. Of the YSO detections, 64 were previously identified in the Getman et al. (2002) study, including 22 of the Class III young stars. Thus we identify 19 new Class III members. Of the cluster members, 41/178 or 23% were identified solely by *Chandra*. A list of the *Spitzer* coordinates and identifiers of the YSOs detected in the *Chandra* field are given in Table 3 along with the evolutionary class and Getman et al. (2002) identifier.

The *Chandra* ACIS-I FOV did not cover the entire *Spitzer* IRAC field. Of the 137 IR-excess YSOs, 127 were in the ACIS FOV: None of the eleven cluster members determined to be in evolutionary Class 0 were detected. Five of the twenty-two Class I protostars were detected ($22.7 \pm 10\%$ of the Class I's in X-ray field of view); eight of the fifteen Flat Spectrum sources were observed ($53.3 \pm 19\%$). Thirty-nine of the seventy-five Class II objects were found to have X-ray counterparts ($52\% \pm 9\%$), while two of the four Transition Disk objects were detected ($50 \pm 35\%$). These are similar detection fractions to the $\sim 50\%$ found in Serpens (Winston et al. 2007). No difference in detection rate was observed between the

later evolutionary classes; to within 1σ , approximately 50% of objects in each of these classes were detected. The X-ray detection fraction in NGC 1333 is slightly lower in the Class I group; however, the protostars in NGC 1333 are more dispersed than in Serpens and tend to lie further off-axis in the ACIS field of view. Compared to the later evolutionary stages, the protostars are more deeply embedded and their soft X-ray emission is more highly absorbed. Further, it is possible that the NGC 1333 protostars are at an early evolutionary stage, the mechanism of X-ray production in these stars may just be turning on in this cluster (Giardino et al. 2007).

3.2. Spatial Distribution

The 178 young stellar objects identified as belonging to the NGC 1333 cluster were mapped to determine their spatial distribution, as shown in Fig. 1. The spatial distribution is shown for the sample of infrared-excess stars (upper two plots) and the sub-sample of X-ray luminous member stars (lower two plots), including the Class III objects. The *Chandra* field of view is constrained to $17' \times 17'$, a region outlined by the four crosses in the figure. A detailed discussion of the underlying distribution of the NGC 1333 YSOs is presented in Gutermuth et al. (2008b, 2009). The protostars in NGC 1333 follow an elongated distribution, tracing the underlying filamentary dust and gas distribution (Hatchell et al. 2005). The Class II and the newly identified Class III stars are more concentrated into a central ‘double’ cluster (Gutermuth et al. 2008b; Lada et al. 1996).

The spatial distribution of the cluster sources was examined for each of the evolutionary classes using a nearest neighbour technique. In keeping with our Serpens study (Winston et al. 2007), the Class 0 and Class I protostars were combined into one group. The nearest neighbour distance is the projected distance to the nearest YSO of the same evolutionary class, using the adopted distance to NGC 1333 of 240 pc. Figure 2 shows the distribution of nearest neighbour distances. We also calculate the nearest neighbor distance for the sub-sample of X-ray detected sources in each evolutionary class. The mean separation between the combined group of Class 0 and Class I protostars is 0.099 pc, with the separation between the Flat Spectrum objects at 0.139 pc. In Serpens, the equivalent separations were 0.033 pc and 0.109 pc, respectively (the Serpens separations are the results from Winston et al. (2007) scaled up to account for the revised distance of 360 pc to Serpens, c.f. Section 4). The Class II sources have a slightly smaller average separation than the protostars of only 0.08 pc (in Serpens 0.134 pc). The separations between the Transition Disk stars have a mean value of 0.437 pc (this is biased by the small number of sources), in Serpens it was 0.183 pc. The mean separation for the Class III stars is 0.097 pc, similar to

that of the youngest protostars. In Serpens, the Class III stars had a mean separation of 0.181 pc, five times that of the protostars. The mean separation of the Class III sources may be biased to a lower value by the field of view of the Chandra data. The X-ray field covers 90% of the Class II sources however, so unless the Class III distribution is greatly extended beyond that of the Class II, then this value is likely a representative result.

Comparison of the spatial distributions of the YSOs in each evolutionary class with a random distribution was carried out by generating 10,000 random distributions with an equal number of stars to that of the given evolutionary class. For the Class III sources the size of the random field is constrained to the *Chandra* field of view. The resulting nearest neighbour distributions were compared using the K-S test and the mean probability taken. The Class I, Class II, and Class III populations were all unlikely to arise from a random distribution with probabilities $< 5 \times 10^{-4}$. The Flat Spectrum and Transition Disk sources had probabilities of 24% and 53%, due to the small number of sources in each class.

In distinct contrast to Serpens, the NGC 1333 star forming region shows a cluster arrangement where the young protostars show a similar spacing to that of the Class II & III populations. It is important to note that the Class II and Class III sources show very similar spacings. We have thus extended the result of Gutermuth et al. (2008a), that the protostars and Class II objects show similar spacings, to the Class III objects. The Kolmogorov-Smirnov probability that the Class II and Class III distributions arise from the same parent distribution is 26.5%. Winston et al. (2009) also find similar age distributions for the Class II and III objects. These observations, taken in aggregate, show that the populations of pre-main sequence stars with and without disks exhibit indistinguishable spatial and age distributions; this suggests that the Class III objects are not typically older, more evolved stars, but stars that lost their optically thick disks more rapidly.

3.3. X-ray Absorption, F_X , and kT of Bright X-ray Sources

The observed X-ray detection limit can be estimated from Feigelson et al. (2005) as $\log(L_X[\text{ergs}^{-1}]) \approx 27.6$, where the distance to NGC 1333 is taken as 240 pc, and the exposure time is 88.45 ks, and the assumed $\log(N_H[\text{cm}^{-2}]) \approx 22$. Only those detections with an X-ray count in excess of 100 were considered when examining the following emission properties to ensure reliable estimates. Fig.3 shows a plot of plasma temperature against the column density of hydrogen. There is a trend with evolutionary class in both kT and N_H , with the Class I sources showing the highest values in both. The Class III sources exhibit the lowest values, from the lowest values we estimate the N_H in the line of sight to the cluster from these diskless sources as $\sim 0.1 \times 10^{22} \text{cm}^{-2}$. The median values of hydrogen column

density by class are: $N_H = 6.12 \pm 8.18 \times 10^{22} \text{ cm}^{-2}$ for the Class I sources and Flat Spectrum sources, $N_H = 0.52 \pm 0.52 \times 10^{22} \text{ cm}^{-2}$ for the Class II and Transition Disk objects, and $N_H = 0.20 \pm 0.43 \times 10^{22} \text{ cm}^{-2}$ for the Class III stars.

Fig.3 shows the X-ray flux corrected for absorption and kT for the different classes. The median flux of the three Class I sources falls in the same range as that of the Class II and III stars, suggesting that the protostellar and PMS X-ray flux levels are similar. Jeffries et al. (2006) have shown increasing kT with flux, and a trend toward cooler coronal temperatures in older clusters. Here, as in Serpens (Winston et al. 2007), the evidence for an increasing trend in the kT to F_X is not clear, with a Spearman rank coefficient of 0.034. If we discard the outliers, those with values of $\log(F_X[\text{erg cm}^{-2} \text{ s}]) < -12.5 \text{ keV}$ and $kT > 5.0 \text{ keV}$, then we obtain a Spearman rank coefficient of 0.33, and a fit of $\log(F_X) \propto 0.47 \pm 0.07 \text{ keV}$, this is equivalent to $\log(F_X) \propto 1.51 \pm 0.21 \text{ keV}$ (MK). The relation for the Serpens data is $\log(F_X) \propto 0.59 \pm 0.14 \text{ keV} \propto 1.82 \pm 0.39 \text{ keV}$ (MK). Previous studies have found values of $\log(F_X) \propto 2.5 \text{ keV}$ (MK) for 1-Temperature model fits to late type stars (Schmitt et al. 1990) and $\log(F_X) \propto 4.0 \text{ keV}$ (MK) for 2-Temperature model of ROSAT solar type field stars (Gudel et al. 1997). Preibisch (1997) finds a value of 2.2 for pre-main sequence stars in the Orion Nebula Cluster, similar to what we find. We defer a more in-depth discussion of the plasma temperature and X-ray luminosities of the Class II and III sources to Section 5.3 where we perform a detailed analysis of the X-ray properties.

3.4. Disk Fraction

To estimate the number of missing diskless Class III objects in our sample, we make an initial assumption that the X-ray detection rates of Class II and Class III sources are similar, at 52%. Further, from the examination of the spatial distribution and nearest neighbour comparisons, we find that, as in Serpens, the spatial distributions of the Class II and III sources are indistinguishable. Hence, as 41 Class III objects were observed, and taking into account that 94% of the Class II population is contained in the *Chandra* field of view, the total Class III YSO population of the cluster may be estimated as $(41/0.52)/0.94$, or 84 objects, which would bring the total cluster membership to 221.

The fraction of stars with disks in the region was calculated from the X-ray detected Class II and III stars, as $39/(41 + 39)$, or $49\% \pm 8\%$, similar to the 51% found in Serpens. If the Class 0/I through Transition Disk objects are included then the fraction becomes: $(5 + 8 + 38 + 2)/(5 + 8 + 38 + 2 + 41)$, or $57\% \pm 8\%$. These fractions may be compared to the disk fraction calculated by Gutermuth et al. (2008b), who subtracted the estimated number of background sources from the observed number of infrared sources in the NGC 1333 field

with $K_S < 14$ mag. This led to an estimate of 87 YSOs in a circular region of radius $5.5'$, covering the same central core as the *Chandra* field, of which 72 were IR-excess YSOs (Class I through Transition Disks), indicating a disk fraction of $72/87$, or $83\% \pm 11\%$. Comparing our X-ray detections in the same circular region, we find 45 IR-excess YSOs and 27 Class IIIs, leading to a disk fraction of $63\% \pm 9\%$. Adopting the same upper K_S -band magnitude limit at 14 mag as Gutermuth et al. (2008b), we find 21 IR-excess YSOs and 15 Class IIIs, giving $58\% \pm 13\%$. The disk fraction estimated by Wilking (1989) of the northern filamentary cluster was $75\% \pm 20\%$. There is a hint that the X-ray selected samples give systematically lower disk fractions than those estimated by source counts, although the 1σ error bars of the results do (barely) overlap. If the number counts method is yielding too high a disk fraction, this may be an underestimate of the number of Class IIIs due to an overestimate of the background contamination in the cluster. Conversely, the assumption that the fraction of Class III detected in X-rays is equal to the fraction of Class II detected may be erroneous. This may be due to the somewhat higher X-ray luminosity in the Class III sources (see Sec. 5.1.)

4. X-ray Luminosity Functions: Distance to Serpens

The X-ray Luminosity Functions (XLFs) of young stellar clusters with ages < 5 Myrs have been found to follow a universal distribution that can be fit by a lognormal with $< \log(L_X[\text{ergs}^{-1}]) > = 29.3$ and $\sigma_{\log(L_X)} = 1$. This has been demonstrated from consideration of observational data from the Orion COUP survey, IC 348, and NGC 1333 (Feigelson & Getman 2005; Feigelson et al. 2005) and LkH α 101 (Wolk et al. 2009). The observed cluster XLF depends only on the number of sources and the distance to the cluster. In Fig.4 we plot the XLF of all the X-ray sources in NGC 1333 with L_X calculated as in Sec.5.1, using the maser parallax derived distance of 240 pc to the cluster (Hirota et al. 2008) and with the log-normal curve overplotted. As was previously reported using less sensitive *Chandra* ACIS-I imaging (Getman et al. 2002), the NGC 1333 luminosity function is well fit by the universal log-normal, indicating that our adopted distance to NGC 1333 is likely to be accurate.

The distance to the Serpens Cloud is currently estimated as 260 pc (Straižys et al. 1996). An early distance determination was that of Strom et al. (1974) who measured the distance to HD 170734 as 440 pc, assuming A0 spectral type, $V = 9.2$ and $E_{B-V} \sim 0.3$. Zhang et al. (1988) reported distance of 700 pc was based on HD 170634, HD 170739, and HD 170784 with B spectral types, and $R = 3.1$. de Lara et al. (1991) used the same stars, adding BD-24607 and Chavarria 7, reclassifying them to be on the main sequence, with $R_{BV} = 3.3 \pm 0.3$

and obtained a distance of 310 pc. Straizys et al. (2003) details Vilnius photometry and photometric classification of 473 stars toward the Serpens Cauda cloud complex, to a depth of $V \sim 13$. The A_V and distance to each star was calculated and used to determine the near edge of the Serpens cloud and to estimate the depth of the cloud. The near edge of the cloud is found to lie at 225 ± 55 pc, with an estimated depth of 80 pc, leading to the average distance of 260 pc. The far edge of the cloud therefore lies at a maximum distance (assuming a $+1\sigma$ deviation) of $225 + 55 + 80 = 360$ pc.

In Fig.5 we plot the XLFs for the Serpens X-ray sources from Winston et al. (2007) with modelled fluxes using four different distances to calculate the luminosity. Three of these are from previous literature studies: 260 pc (the currently most commonly adopted distance), 310 pc, and 440 pc, and one at 360 pc. We performed a least squares fit of the observed distribution to the universal XLF of Getman et al. (2005), varying the number of sources between 39 and 81 members and incrementing the distance by 10 pc from 250 to 450 pc. The fit was performed on the tail of the distribution from $\log(L_X) \geq 29.3$ to avoid including any incomplete luminosity bins in the sample and to fit to the universal XLF where it is best defined. The figure shows the minimum χ^2 fit at each distance and the fit for 60 sources, the χ^2 probabilities for both fits are also given. The best fit to the data was found to be at a distance to Serpens of 360^{+22}_{-13} pc and 60 detections, with a χ^2 probability of 0.998. To estimate the uncertainties, we determine the distances at which $\chi^2 = \min(\chi^2) \pm 1$ while constraining the number of objects to 60 and varying the distance in steps of 1 pc. There are 60 *Chandra* detections coincident with IR sources in the Serpens field, though only 40 had high enough count rates to have luminosities determined through model spectrum fits (hence the flat topped observed luminosity distributions in Fig.5). As such, the model fit to sixty sources appears to be reasonable. We note that if the number of X-ray luminous members is in excess of 60, higher distances are likely. For example, a high probability of 0.9 is found for 40 pc *if* we allow 80 objects - 20 more than have been detected. In contrast, distances of 310 pc or lower require the numbers of X-ray luminous members to be *less* than the number detected and may be ruled out. This best fit distance is approximately mid-way between the de Lara et al. (1991) 310 pc and Strom et al. (1974) 440 pc estimates, and indicates that Serpens may be further than the commonly adopted 260 pc. While statistical uncertainties and systematic errors in the determination of L_X will introduce scatter and cause uncertainty in the XLF fitting, and the universal XLF itself is not exactly lognormal, these errors should apply equally to NGC 1333. As NGC 1333 is consistent with the universal XLF for the known distance and cluster membership, we find it unlikely that the more distant fit of Serpens can be due to these effects alone. Given that similar velocities have been found for the molecular gas associated with the recently discovered Serpens South cluster (Gutermuth et al. 2008a) and that associated with the Serpens Cloud Core studied here, we suggest that this further

distance apply to the southern region as well.

To ascertain whether this new estimated distance is compatible with our previous study of the Serpens HR diagram (HRD), in Fig.6 we have replotted the HRD of the region using the distance of 360 pc to calculate the luminosities of the spectrally classified YSOs (c.f. Fig.6 in Winston et al. (2009) for the HRD at 260 pc). At the new distance, the median age of both the Class II and III YSOs decrease to 1 Myrs. Two objects are newly located at or above the birth line, and these may be over-luminous, perhaps due to binarity, variability, or uncertainties in the position of the birthline. The majority of sources now have isochronal ages less than 3 Myr. At this distance, only four members now have apparent isochronal ages >10 Myr and none have ages >30 Myr. These ages are more in keeping with what might be expected of YSOs in a deeply embedded cluster rich with protostars. In the following discussions in this paper, both the bolometric and the X-ray luminosities for the Serpens cluster have been calculated from this new distance of 360 pc.

Does the XLF depend on evolutionary class? Fig.7 shows the XLFs of the two clusters by evolutionary class for the Class II, Class III, and protostellar sources (Class I and Flat Spectrum). In both clusters the Class II and Class III members show similar XLFs, with a Kolmogorov-Smirnov test probability of their arising from the same parent distribution of 48% in NGC 1333 and 65% in Serpens, for sources with $\log(L_X[\text{ergs}^{-1}]) \geq 29$ in Serpens and ≥ 28.5 in NGC 1333. These cut-offs in luminosity are imposed so that the K-S tests are based on complete bins in all evolutionary groups. The K-S probabilities indicate that the detection rate of the Class III sources is comparable to that of the Class II. This is similar to Getman et al. (2002), who found no differences in the XLFs of the Class II and Class III sources in the ONC. In contrast, Telleschi et. al. (2007) show WTTS to be brighter in X-rays than CTTS in Taurus. In Section 5.2 we will further discuss the differences in Class II and III X-ray luminosities.

The protostellar sources also show similar XLFs to those of the more evolved objects, although the sample is biased towards higher luminosities by their higher extinctions. In NGC 1333, the XLFs have probabilities of 71% and 34% of being drawn from the same parent distribution as the Class II and III sources, respectively. In Serpens, those probabilities are 99% and 86% for Class II and III sources, respectively. Thus, we find no evidence that the protostellar luminosity function differs from the primarily Class I and Flat Spectrum sources.

5. The Dependence of X-ray Emission on Measured Stellar Properties

5.1. X-ray Luminosity and Bolometric Luminosity

While the X-ray luminosity of main sequence stars, like the Sun, is variable, it also scales as a function of the bolometric luminosity and is dependent on the Rossby number (a measure of the stellar rotation rate) and the convective turnover time (Noyes et al. 1984). The X-ray luminosity of pre-main sequence stars has also been found to vary with bolometric luminosity (Feigelson et al. 1993; Preibisch et al. 2005). Coronal magnetic activity appears to be less variable in pre-MS stars than in MS stars (Stern et al. 1994), and is likely the origin of most of the X-ray emission from the YSOs, though accretion processes may also have an effect. Preibisch et al. (2005) and Preibisch & Zinnecker (2002) examined the relation of L_X to L_{bol} for YSOs in the Orion COUP survey and IC 348, and for a sub-sample of field stars from the NEXXUS survey. They find that for pre-main sequence stars $L_X \propto L_{bol}^\alpha$, where $\alpha \sim 1$, compared to $\alpha \sim 0.4$ for stars on main sequence. This relation was also observed for pre-main sequence stars in the Taurus molecular cloud by the XEST survey (Telleschi et al. 2007).

We applied a similar analysis, determining the X-ray luminosity from $L_X = 4\pi D^2 F_X$ where D is the distance (we use F_X tabulated in Table 1 for NGC 1333 and on the ANCHORS website for Serpens, using our new estimate of the distance in the calculation), and using the L_{bol} from Winston et al. (2007). Tables 4 & 5 list the spectral, X-ray and IR properties of the 138 YSOs considered in the following studies. The tables list the *Spitzer* identifier, spectral type, evolutionary class, *Chandra* identifier, bolometric luminosity, effective temperature, stellar surface area, the X-ray luminosity, plasma temperature and hydrogen column density, the extinction at K -band, isochronal age and mass. The Serpens data are taken from Winston et al. (2007) and Winston et al. (2009), while the NGC 1333 IR and spectroscopic data are taken from Gutermuth et al. (2008a) and Winston et al. (2009), and the NGC 1333 X-ray data from this work. The isochronal ages and masses were determined from the isochrones and mass tracks of Baraffe (1998) interpolated onto a grid using IDL routines; the earliest isochrone used was 1 Myr. Those sources with isochronal ages listed as ~ 0.2 Myr were near to the boundary of the grid used for extrapolation, where the age estimates were less certain, and were therefore assigned an estimated isochronal age. Those without an isochronal age or mass measurement were located beyond the boundaries of the grids where a useful age/mass estimate could not be obtained. The extinction at K -band was measured following Gutermuth et al. (2008a) - who uses the CTTS locus first discussed by Meyer et al. (1997). Where a value of K -band extinction could not be determined or was found to be blueward of the CTTS locus, the A_K was set to zero in the calculations. In Tables 4 & 5 an A_K of 0. indicates that the source was blueward of the CTTS locus, and a

null value that it could not be calculated.

Figure 8 plots the stellar X-ray luminosity against the stellar bolometric luminosity in units of L_\odot for the Serpens (left) and NGC 1333 (right) clusters. In both regions, a trend of increasing L_X with stellar bolometric luminosity is observed. The slope of the relationship in the Serpens data is: $\log(L_X[\text{ergs}^{-1}]) \propto (0.82 \pm 0.11) \log(L_*/L_\odot)$, and the slope in the NGC 1333 region is: $\log(L_X[\text{ergs}^{-1}]) \propto (0.91 \pm 0.10) \log(L_*/L_\odot)$. In both regions, the bolometric values correspond, within 2σ , to the $L_X \propto L_{bol}$ relation observed previously in other young stellar clusters. For the NGC 1333 region, the Class II sources appear slightly less luminous than the Class III, but with the large scatter in the data the difference is less than 1σ . The power law exponent for the Class II sources is: $\log(L_X[\text{ergs}^{-1}]) = 29.69 \pm 0.10 + (0.98 \pm 0.13) \log(L_*/L_\odot)$, while for the Class III sources it is: $\log(L_X[\text{ergs}^{-1}]) = 29.85 \pm 0.19 + (0.86 \pm 0.14) \log(L_*/L_\odot)$.

In Winston et al. (2007), a discussion of the stellar X-ray flux to the dereddened J -band magnitude was put forth. The near-IR magnitude was used as a proxy for the stellar bolometric luminosity. In Serpens and NGC 1333, respectively, we find values of $F_X \propto m_J^\alpha(\text{dered})$ with α of 0.42 ± 0.17 and 0.53 ± 0.09 , where $m_J(\text{dered})$ is the dereddened magnitude. Casanova et al. (1995), working from the results of Greene et al. (1994), found empirically that $\log(L_{bol}/L_\odot) \propto -0.4m_J(\text{dered})$. Therefore, the F_X vs. $m_J(\text{dered})$ relationships are consistent with our derived L_{bol} and L_X relationships.

5.2. L_X with Surface Area & Effective Temperature

In this section we will examine the dependence of L_X with surface area and with T_{eff} to discover if the increasing trend of X-ray flux to bolometric luminosity arises from variations in the effective temperature or the surface area of the star. The bolometric luminosity of a star may be given as $L_{bol} = 4\pi R^2 \sigma T_{eff}^4$, where $4\pi R^2$ is the stellar surface area and T_{eff} is the effective temperature. The surface area was determined in solar units from the bolometric luminosity and effective temperature derived from the spectral classification of each star, determined in Winston et al. (2009). The plots in Figs. 9 & 10 examine the physical parameters on which the L_X vs. L_{bol} relation may depend: stellar surface area, $S.A.$, and effective temperature, T_{eff} . We note that the stellar surface area and effective temperature are not independent parameters: they will show some interdependence, such that hotter, more massive pre-main sequence stars will on average have larger surface areas.

In Fig. 9, the X-ray luminosity is plotted against the stellar surface area. The trend to increasing L_X with stellar surface area is clearly visible in the plots. In Serpens, the fit to

these data is $\log(L_X[\text{ergs}^{-1}]) = 28.74 \pm 0.13 + (1.09 \pm 0.10) \log(SA_*/SA_{sol})$, while in NGC 1333 it is $\log(L_X[\text{ergs}^{-1}]) = 28.85 \pm 0.09 + (1.34 \pm 0.12) \log(SA_*/SA_{sol})$. In Serpens, the Class II and III YSOs do not show any difference in trend of L_X to $\log(SA_*/SA_{sol})$. In NGC 1333, for a given surface area, the Class III YSOs have a somewhat higher X-ray flux than the Class IIs. The two populations can be fitted separately, with $\log(L_X[\text{ergs}^{-1}]) = 28.65 \pm 0.13 + (1.42 \pm 0.18) \log(SA_*/SA_{sol})$ for the Class III and $\log(L_X[\text{ergs}^{-1}]) = 29.06 \pm 0.10 + (1.24 \pm 0.16) \log(SA_*/SA_{sol})$ for the Class II. This difference in the median luminosity of the two fits is approximately 0.3 dex. Thus, we find a marginal offset of about 2σ between the fits of the two evolutionary classes. It is not clear why Serpens and NGC 1333 show different results. We do note that the Serpens sample is smaller (12 Class II and 11 Class III vs. 31 Class II and 23 Class III in NGC 1333) and dominated by more X-ray luminous objects where the difference between Class II and III objects is less obvious; hence such a difference could be less apparent.

In Fig. 10, the X-ray luminosity is compared with the effective temperature, T_{eff} . In order to remove the contribution from surface area and thus isochronal age, the surface area has been divided out of the X-ray luminosity data to give the surface flux: $L_X/(SA_*/SA_{sol})$. The overlaid graphs plot the median value of $L_X/(SA_*/SA_{sol})$ in bins of 500 K in T_{eff} from 2500 K to 6000 K. There is a discontinuity in the NGC 1333 plot, which occurs at an approximate temperature of 3800K, the transition between *M0* and *K7* spectral types. A Kolmogorov-Smirnov test was performed on the populations to either side of this boundary temperature to ascertain the probability that they are from the same parent distribution: in NGC 1333 the probability was 7.4%, in Serpens 29.3%. Although the result in NGC 1333 is suggestive, a larger sample of sources is needed to provide the statistical significance necessary to confirm the discontinuity.

Previous studies have arrived at contradictory answers on the issue of the X-ray luminosity of Class II and Class III YSOs. A number of studies have found no difference in the X-ray luminosities of the two groups (Gagné et al. 1995; Feigelson et al. 1993; Casanova et al. 1995; Preibisch & Zinnecker 2002), while in Taurus, Stelzer & Neuhauser (2001) and Telleschi et. al. (2007) find the WTTS to be more luminous. Preibisch et al. (2005) find that while accreting T Tauri stars are less luminous than non-accretors, those stars with *K*- or *L*-band excesses show no difference in luminosity to those without. It is not clear how much of this is due to the intrinsic scatter in the X-ray luminosities (which is greater than the systematic differences between Class II and III sources), real differences between different star forming regions, and the different criteria (accretion signatures and near IR excess emission) used to separate Class II and Class III. Winston et al. (2009) found a strong correspondence between the presence of an accretion indicator and the presence of an IR-excess from a disk; thus, we do not expect a difference in behavior between samples

selected by accretion indicators and those selected by IR-excess. The fact that even with the *Spitzer* data, we find one cluster with differing Class II and II X-ray luminosities (NGC 1333) and one without (Serpens) suggests that the contradictory results may result from a combination of the large intrinsic scatter and the smaller sample size in Serpens.

Given the dependence of L_X on surface area for detected sources, it is also important to assess the detection rate of YSOs as a function of their surface areas. In Fig.11, the histograms of the surface areas of the Class II and Class III YSOs with spectral types in each cluster are presented for both clusters. The solid black histograms indicate the X-ray detected YSOs, while the shaded grey histograms are those of the non X-ray detections. The Class II sources without X-ray detections are easily detected by their IR-excesses. The displayed sample are the Class II sources for which we obtained spectra; Winston et al. (2009) describe the selection biases in that sample. The histograms show that the X-ray detected Class IIs have larger surface areas than the non X-ray detections, with median values of 2.62 and 0.61 $S.A._{\odot}$ for NGC 1333 and 3.32 and 0.70 $S.A._{\odot}$ for Serpens, respectively. The Class IIIs have median values of 1.94 $S.A._{\odot}$ for NGC 1333 and 2.35 SA_*/SA_{sol} for Serpens. To attempt to find a value for the non X-ray detected Class IIIs we have utilised the candidate Class IIIs identified from *Li I* in their spectra (Winston et al. 2009). Their median surface areas were 1.11 and 1.54 SA_*/SA_{sol} for NGC 1333 and Serpens, respectively, though the statistics here are small. Not only are the median surface areas of the non-detected sources smaller, but we find that all of the non-detected sources have $\log(SA_*/SA_{sol}) < 1$ for Serpens and < 0.5 for NGC 1333. Such sources with smaller surface areas may emit too weakly in X-rays to be detected in our *Chandra* observations unless they are undergoing strong flaring.

5.3. Plasma Temperature with Surface Area and Effective Temperature

In Section 3, the X-ray luminosity was found to increase with the plasma temperature. A hotter plasma may arise from increased heating rate in the coronal loop or through increased loop length (Preibisch 1997). Gagné et al. (1995) note that the plasma temperature is dependent on the stellar rotation period and stellar age. Preibisch et al. (2005) also find that the plasma temperature increases with T_{eff} . As L_X is dependent on SA and T_{eff} , in Fig. 12, we investigate the dependence of the X-ray plasma temperature, kT , on the surface area and effective temperature of the star. The fits to these plots were made while removing the outlier data points: the outlier points are at $kT \approx 6$ keV in Serpens, and at $kT > 3$ keV in NGC 1333 (see the kT vs SA plot in Fig. 12 for the motivation for removing these points.) Neither cluster shows strong evidence of a trend in plasma temperature with increasing effective temperature. Both clusters do show trends of increasing plasma

temperature with increasing surface area. The Serpens data show a trend of $kT[keV] = 0.85 \pm 0.22 + (2.02 \pm 0.28) \log(SA_*/SA_{sol})$, with NGC 1333 giving $kT[keV] = 1.09 \pm 0.26 + (1.76 \pm 0.22) \log(SA_*/SA_{sol})$.

There is also a dependence of plasma temperature on evolutionary class. In NGC 1333, the Class II and Class III sources have statistically distinguishable values of kT , with a Kolmogorov-Smirnov test giving a probability of 3.3% that the Class II and III come from the same distribution (in Serpens the probability is 21%, probably due to the small sample). A similar difference in the electron temperature of CTTS and WTTS was observed in the Taurus XEST study by Telleschi et. al. (2007). In NGC 1333, the mean value of the Class II is $kT = 2.41 \pm 1.19$ keV and the mean value for the Class III sources is $kT = 1.12 \pm 0.59$ keV. The mean value for the 3 Class I objects is $kT = 3.95 \pm 2.85$ keV, though the Class I objects likely have higher extinctions that may absorb most of the low energy X-rays. All but one of the Class III diskless members have plasma temperatures ≤ 2.5 keV, while the Class I sources all exhibit kT values above 3 keV.

5.4. X-Ray Luminosity with Isochronal Age and Mass

It is known that L_X decreases with age over the stellar lifetime and increases with stellar mass (Micela et al. 2002a,b). The ages and masses of the stars in Serpens and NGC 1333 were determined by use of their spectral types to map them from the H-R diagram with isochrones and mass tracks taken from Baraffe (1998), and are thus dependent on the choice of model. The apparent isochronal ages and the inferred age spreads, in particular, are controversial (Chabrier et al. 2000; Hartmann et al. 2005; Peterson et al. 2008; Winston et al. 2009). We do not expect to see evidence for a rapid decrease in L_X with age over the isochronal ages of these stars; other cluster studies have shown that the X-ray luminosity does not decrease rapidly until ~ 100 Myrs (Micela et al. 2002a). A decreasing trend in X-ray luminosity with stellar age was found for PMS stars in Orion by Preibisch & Feigelson (2005). Given their large sample, they use four mass bins from 0.1 to $2 M_\odot$, while here we will examine the sample as a whole. Over all four bins, they find a decreasing trend of L_X with age, with average value: $\log(L_X[ergs^{-1}]) \propto (-0.30 \pm 0.13) \log(\tau[Myr])$.

Figure 13 (left) examines the X-ray luminosities of the young stars with respect to their ages. A marginal trend towards lower luminosities with increasing age is observed in the NGC 1333 data, $\log(L_X[ergs^{-1}]) \propto (-0.32 \pm 0.17) \log(\tau[Myr])$, while no significant trend is found in the Serpens region. Since stars contract as they age, this may result from the dependence of X-ray luminosity on the surface area. No difference was observed in the fits of L_X with isochronal age separated by evolutionary class.

Preibisch & Zinnecker (2002) found in IC 348 that the $L_X \propto M^\alpha$ where $\alpha = 2$, whereas Preibisch et al. (2005) found a lower α of 1.44 or 1.13 for stars with mass $< 2 M_\odot$ in Orion (depending on whether the Siess et al. (2000) or Palla & Stahler (2000) PMS model tracks, respectively, are used). Work in Taurus by Telleschi et. al. (2007) on the *XEST* survey found $\alpha = 1.49 \pm 0.07 \log(M/M_\odot)$. Figure 13 (right) examines the effect of stellar mass on the X-ray luminosity; the masses were determined by Winston et al. (2009) using the Baraffe (1998) tracks. A trend to increasing L_X with increasing mass is evident in NGC 1333, with $\alpha = 0.99 \pm 0.16$. In Serpens $\alpha = 0.12 \pm 0.21$, we do not find a significant increase with mass. The trends with mass were not found to be dependent on evolutionary class.

5.5. Discussion of X-ray Properties

From our analysis of the X-ray and spectral properties of the two clusters NGC 1333 and Serpens we identify four main relations of interest that we will discuss in this section.

Dependence of X-ray Luminosity on Bolometric Luminosity & Stellar Surface Area. In Sec 5.1 we find that the L_X v. L_{bol} relation holds to that published in the literature for other young stellar clusters in Serpens and NGC 1333. In the young stars, $\log(L_X)$ increases approximately linearly with $\log(L_{bol})$, while for more evolved field stars the relation is shallower. We find that the strong dependance of L_X on bolometric luminosity is due for the most part to an approximately linear dependence on the surface areas of the young stars, while there is a much weaker dependence with effective temperatures. The dependence on surface area suggests that coronal X-ray production is saturated in the young stars. Further, this dependence suggests that coronal emission (and not accretion emission) is the dominant mechanism involved in X-ray production in the YSOs.

Dependence of X-ray Luminosity on Evolutionary Class. We use our IR SED classifications of Class II and Class III objects to compare the properties of diskless and disk-bearing YSOs and find that for a given surface area the Class III stars are more X-ray luminous than the Class II.

In NGC 1333, we find some evidence that for a given surface area, the mean luminosity of the Class III YSOs is somewhat higher than that of the Class IIs. The difference between the median Class II and Class III values is ~ 0.3 dex. Such a difference has been noted previously in other regions and suggested explanations include: absorption of X-rays due to the inclination of the circumstellar disk in Class II sources, or magnetic disk-braking causing slower rotation in Class IIs and thus a weaker α - ω dynamo. It is also possible that the accretion column onto the surface of the Class II stars is reducing the total volume

of the corona available to produce X-rays (Gregory et al. 2007). This would require that $\sim 30\%$ ($0.3\ dex$) of the surface area of the Class II stars was covered by accretion columns. However, studies such as Calvet & Gullbring (1998) and Muzerolle et al. (2001) estimate that from 1%-10% of the stellar surface is affected by accretion. This effect is therefore not large enough to fully account for the difference between the Class II and III stars.

Another possible origin of the difference in Class II and III L_X for a given L_{bol} or SA is that the disk-bearing YSOs are over-luminous in L_{bol} due to veiling, which leads to an over estimation of their bolometric luminosity (Cieza et al. 2005). In Winston et al. (2009) we estimate veiling of up to $0.3\ dex$ in L_{bol} . However, if this were the case the Class II would be systematically intrinsically fainter than the Class III (by $\sim 0.3\ dex$) and would therefore have a greater median age (~ 4.5 Myr compared with the current ~ 2.1 Myr), making them significantly older than the Class III (~ 2.4 Myr).

Dependence of X-ray Luminosity on Effective Temperature. In NGC 1333, we find some evidence for a discontinuity in the distribution of X-ray luminosities at 3800 K, the boundary between K7 and M0 spectral classes. The K-M boundary at 1 Myr is the approximate location of the turnover from the convection tracks to the radiative tracks (Baraffe 1998). The discontinuity in X-ray luminosity could then be due to the transition between the fully convective YSOs and those developing a radiative core and convection zone.

Dependence of Plasma Temperature with Evolutionary Class, Surface Area, Effective Temperature We find that the plasma temperature increases with the surface area squared, but there is no apparent dependence on effective temperature. In NGC 1333, the Class III stars exhibit consistently cooler plasma temperatures than the Class II. This is also seen to a lesser extent in Serpens where the Class III objects do not show plasma temperatures exceeding ~ 2.5 keV. If the plasma temperature is dependent on the coronal loop length, this might imply that the Class II stars had longer loop lengths. However, the higher plasma temperature and lower luminosities of Class II objects may be due to under-correction of disk absorption in the X-ray modelling, thus leading to hotter plasma temperatures (since the lower energy X-rays are absorbed) and lower L_X determinations for the Class IIs.

Dependence of X-ray Luminosity on Isochronal Age & Mass. Lastly, we find some weak dependence of X-ray luminosity with isochronal age and mass, qualitatively consistent with dependence on surface area and effective temperature, from which the values of age and mass are determined. The X-ray luminosity tends to decrease slightly if at all with isochronal age and to increase with mass. Since the isochronal age depends on surface area, the dependence of L_X with age may really be the dependence of L_X with stellar

surface area. In turn, the surface area depends in part on age, mass, and potentially the accretion history (Chabrier et al. 2009), thus weakening the dependence on the actual age of the source. The dependence of L_X with stellar mass may also reflect the dependence with surface area, although the possible increase of L_X with T_{eff} may also contribute.

6. Hydrogen Column Density and Extinction in NGC 1333 and Serpens

The X-ray and infrared results have also been used to calibrate the relationship between Hydrogen gas column density in the line of sight and the extinction measured using the near-IR bands (Fig. 14). Previous measurements of this value lead to an approximately linear fit of $1.6 \times 10^{21} A_V$ (Vuong et al. 2003; Feigelson et al. 2005) for star forming regions, while the value for the diffuse ISM ranges from $1.8 - 2.2 \times 10^{21} A_V$ (Vuong et al. 2003; Gorenstein 1975). In NGC 1333, Preibisch (2003) noted that SVS16 had a value of N_H corresponding to an $A_V \sim 10$ mag inconsistent with the extinction calculated in the IR of $A_V \sim 26 - 28$ mag and suggested this may be due to the X-ray production mechanism or a change in the canonical dust-to-gas ratio. Winston et al. (2007) found the value using Class III objects in the Serpens region $N_H = 0.63 \pm 0.23 \times 10^{22} A_K$, where $A_K \sim 1/10 A_V$ (Rieke & Lebosky 1985). The rationale for using the Class III objects was that they would be unaffected by local extinction due to disks and accretion flows. Winston et al. (2007) proposed that this discrepant value was due to changes in the extinction law due to the growth of grains through the accretion of volatiles onto grain mantles and/or coagulation. A limitation of this result was that the fit of the extinction law was driven by only three Class III objects with $1.6 > A_K > 2.4$.

We calculated A_K for each star using the method of Gutermuth et al. (2004), which is based on the reddening loci from Meyer et al. (1997) and the extinction law of Flaherty et al. (2007). These values are compared to the column density of hydrogen atoms, N_H , which is calculated from the inferred absorption of the X-ray emission for 26 objects in NGC 1333 and 18 in Serpens. The results for NGC 1333 are consistent with those in Serpens by Winston et al. (2007). The linear fit of the slope for seven Class III stars was $N_H = 0.89 \pm 0.13 \times 10^{22} A_K$, while that for the Class II objects (18 in number) was $N_H = 0.87 \pm 0.17 \times 10^{22} A_K$. In all cases, the ratio falls below that found for the diffuse ISM (Vuong et al. 2003). In the Class II objects, the X-rays may be absorbed by the gas in an accretion flow (within which it would be too hot for dust grains to exist) or in a disk. In addition, some of the near-IR light might be scattered by dust in the disks, potentially resulting in an underestimate of the extinction. This would be consistent with our analysis in Sec. 3, which shows a lower X-ray luminosity and higher X-ray temperature for the Class II sources

compared to the Class III sources. Since the N_H v. A_K relationship for Class II objects could be affected by the circumstellar environment, it is best determined using Class III objects. These diskless sources are reliably identified with the mid-IR data from *Spitzer*.

The relationship of N_H to A_K was previously examined in the NGC 1333 region by Getman et al. (2002) using an 37.5 ks *Chandra* observation of the region. While they find their results to be consistent with standard ISM values, they also note that some sources are consistent with the lower N_H v A_K slope we determined from the Serpens region. We have compared their values of N_H and A_V to our own and found that they agree to within the 1σ uncertainties. In our work, the low N_H vs. A_K slope becomes apparent due to the separation of sources into Classes II and III and our extension to higher A_K .

For the combined clusters, the slope of N_H to A_K is $\sim 1/3$ that of the interstellar ISM. Using the Class III objects of NGC 1333 and Serpens, we calculate that $N_H = 0.79 \pm 0.19 \times 10^{22} A_K$. These results are consistent with those found in the deeply embedded stars in the RCW 108 region (Wolk et al. 2009), suggesting that the slope of N_H v A_K is typically lower in deeply embedded regions where the extinction exceeds $1 A_K$.

7. Conclusion

In this paper we have presented *Chandra* X-ray observations of the NGC 1333 star forming region, and compared these data with the *Spitzer* catalogue of identified young stellar objects in the region. The work further presents a comparative study of the X-ray and fundamental stellar (bolometric luminosity, effective temperature, age, mass) properties of the NGC 1333 and Serpens clusters determined with far-red and near-IR spectra.

- In total, we identify 95 NGC 1333 cluster members in X-rays. Five of these detections were Class I, eight Flat Spectrum, thirty-nine Class II, and two Transition Disk objects. We identify 41 Class III members of the NGC 1333 cluster through their elevated X-ray emission, 19 of which are new to this study. This brings the total number of detected cluster members to 178.
- We found the fraction of each class detected in X-rays; 23% of Class I, 53% of Flat Spectrum, 52% of Class II, 50% of Transition Disks. If the detection rate of Class II and Class III sources are the same, the total Class III population of the cluster is approximately 84 members (implying 221 members in total); however, if the Class III sources are more X-ray luminous than the Class II sources then the number of Class III sources will be lower. None of the known Class 0 protostars were detected by *Chandra*.

- Using the XLF of Serpens, a new distance to the cluster is estimated at 360^{+22}_{-13} pc. This distance is similar to previous literature distances to the cluster, and is found to be compatible with the HRD of the region, giving a median age of 1 Myr for the star forming region. This new distance may also be applied to the recently discovered Serpens South cluster.
- The $L_X \propto L_{bol}$ relation found in other star forming regions was confirmed for the two clusters. This was found to be predominantly a dependence of X-ray luminosity on the stellar surface area, with some weak dependence on the effective temperature. There is some evidence for a jump in L_X with T_{eff} near the M0-K7 transition, which may be due to the turnover from purely convective YSOs to one with a developing radiative core.
- A marginal dependence of X-ray luminosity with evolutionary class suggests that the diskless Class III sources in NGC 1333 are, for a given stellar surface area, more luminous than their disk-bearing Class II counterparts. In Serpens the two classes show similar luminosities, although this may be due to the smaller sample size and the larger scatter.
- The temperature of the X-ray emitting plasma was also examined as a function of effective temperature and surface area, with increasing trends observed with surface area. The Class III sources are found to have lower values of kT than the Class II in each case, with K-S probabilities of them arising from the same distribution of 21% (Serpens) and 3.3% (NGC 1333). This may be a result of underestimation of the absorption due to circumstellar disks.
- The variation of X-ray luminosity with age was considered, indicating a marginal trend in NGC 1333 to higher levels of X-ray flux at younger ages. This may reflect the dependence of isochronal age on stellar surface area. There is also a trend in F_X with mass, with more massive YSOs showing higher X-ray fluxes. This is consistent with previous studies such as the *COUP* in Orion.
- In the case of NGC 1333, the ratio of N_H to A_K is lower than expected, $N_H = 0.89 \pm 0.13 \times 10^{22} A_K$, a similar value to that found in Serpens (Winston et al. 2007). The median value for both clusters is $N_H = 0.79 \pm 0.19 \times 10^{22} A_K$. This may be the result of grain growth through coagulation of the accretion of grain mantles as discussed in Winston et al. (2007).

This work is based on observations made with the *Chandra* Telescope, under NASA contract NAS8-03060. This work is based on observations made with the *Spitzer* Space

Telescope (PID 6, PID 174), which is operated by the Jet Propulsion Laboratory, California Institute of Technology under NASA contract 1407. Support for this work was provided by NASA through contract 1256790 issued by JPL/Caltech. Support for the IRAC instrument was provided by NASA through contract 960541 issued by JPL. This work is based on observations taken with the *Hectospec* instrument on the MMT, a joint venture of the Smithsonian Institution and the University of Arizona. This publication makes use of data products from the Two Micron All Sky Survey, which is a joint project of the University of Massachusetts and the Infrared Processing and Analysis Center/California Institute of Technology, funded by the National Aeronautics and Space Administration and the National Science Foundation. This research has made use of the NASA/IPAC Infrared Science Archive, which is operated by the Jet Propulsion Laboratory, California Institute of Technology, under contract with the National Aeronautics and Space Administration.

REFERENCES

- Allen, C., Jerius, D. H., & Gaetz, T. J. 2004, *Proc. SPIE*, 5165, 423
- Aspin, C., Sandell, G., Russell, A.P.G., 1994, *A&AS*, 106, 165.
- Baraffe, I., 1998, *A&A*, 337, 403,
- Calvet, N., Gullbring, E., 1998, *ApJ*, 509, 802.
- Casanova, S., Montmerle, T., Feigelson, E.D., Andre, P., 1995, *ApJ*, 439, 752.
- Chabrier, G., Baraffe, I., Allard, F., Hauschildt, P., 2000, *ApJ*, 542, 464.
- Chabrier, G., Baraffe, I., Allard, F., 2009, *in press*.
- Cieza, L., et al., 2005, *ApJ*, 635, 422.
- D’Antona, F., Mazzitelli, I., 1997, *Mem. S.A.It.*, 68, 807.
- Davis, C.J., Matthews H.E., Ray T.P., et al, 1999, *Mon. Not. R. Astron. Soc* 309, 141-152.
- de Lara, E., Chavarria, K. C., Lopez-Molina, G. 1991, *A&A*, 243, 139.
- Favata, et al., 2003, *A&A*, 403, 187.
- Favata, et al. , 2005, *ApJS*, 160, 469.
- Fazio, G.G., et al., 2004, *ApJS*, 154, 10.
- Feigelson, E., Getman, R., et al., 2005, *ApJ*, 160, 379.
- Feigelson, E. & Getman, R., 2005, *astro-ph/0501207*.
- Feigelson, E. D., Montmerle, T., 1999, *ARA&A*, 37, 363-408.
- Feigelson, E.D., Casanova, S., Montmerle, T., Guibert, J., 1993, *ApJ*, 416, 623.
- Feigelson, E. D.; Kriss, G. A., 1981, *ApJ*, 248, L35-L38.
- Flaherty, K.M., et al., 2007, *ApJ*, 663, 1069F.
- Gagné, M., Caillaut, J.P., Stauffer, J.R., 1995, *ApJ*, 450, 217.
- Getman, K.V., et al., 2008, *ApJ*, 688, 437.
- Getman, K. V., et al., 2005, *ApJS*, 160, 319-352.

- Getman, K. V., et al., 2002, *ApJ*, 575, 345-377.
- Giampapa, M.S., et al., 1996, *ApJ*, 463, 707.
- Giardino, G., Favata, F., Micela, G., Sciortino, S., Winston E., 2007, *A&A*, 463, 275-288.
- Gorenstein, P., 1975, *ApJ*, 198, 95.
- Greene, T.P., Wilking, B.A., Andre, P., Young, E.T., Lada, C.J., 1994, *ApJ*, 434, 614.
- Gregory, S.G., Wood, K., Jardine, M., 2007, *MNRAS*, 379, L35-L39.
- Gudel, M., Guinan, E.F., Skinner, S.L., 1997, *ApJ*, 483, 947.
- Gutermuth, R., et al., 2009, *ApJS*, 184, 18G.
- Gutermuth, R., et al., 2008, *ApJ*, 673, 151.
- Gutermuth, R., et al., 2008, *ApJ*, 674, 336.
- Gutermuth, R., Megeath, S. T., Muzerolle, J., Allen, L., Pipher, J., Myers, P., Fazio, G. G., 2004, *ApJS*, 154, 374.
- Hatchell, J., et al., 2005, *A&A*, 440, 151-161.
- Hartmann, L., Megeath, S.T., Allen, L.E., Luhman, K., Calvet, N., D'Alessio, P., Franco-Hernandez, R., Fazio, G., 2005, *ApJ*, 629, 881-896.
- Hayashi, M.R., Hibata, K., Matsumoto, R., 1996, *ApJ*, 468, L37.
- Hernandez, J., et al., 2007, *ApJ*, 662, 1067.
- Hirota T., et al., 2008, *PASJ*, 60, 37.
- Hogerheijde, M., van Dishoeck E., Salverda J., 1999, *ApJ*, 513, 350-369.
- Isobe, H., et.al., 2003, *PASJ*, 55, 967.
- Jeffries, R.D., Evans, P.A., Pye, J.P., Briggs, K.R., 2006, *Mon. Not. R. Astron. Soc.*, 367, 781-800.
- Kaas, A.A., Olofsson G., Bontemps S., et al, 2004, *A&A*, 421, 623-642.
- Kastner, J.H., et al., 2002, *ApJ*, 567, 434.
- Knee, L.B.G., & Sandell, G., 2000, *A&A*, 361, 671.

- Küker, M., & Rüdiger, G., 1999, A&A, 346, 922.
- Lada, C.J., Alves, J., Lada, E.A., 1996, AJ, 111, 1964.
- Mercer, E.P., et al., 2009, AJ, 138, 7-18.
- Meyer, M. R.; Calvet, N.; Hillenbrand, L. A., 1997, AJ, 114, 288-300.
- Micela, G., et al., 2002, ASPC, 269, 107.
- Micela, G., et al., 2002, ASPC, 277, 263.
- Muzerolle, J., Calvet, N., Hartmann, L., 2001, ApJ, 550, 944.
- Noyes, R.W., Hartmann, L.W., Baliunas, S.L., et al., 1984, ApJ, 279, 763.
- Palla, F., Stahler, S.W., 1999, ApJ, 525, 772.
- Peterson, D.E., et al., 2008, ApJ, 685, 313.
- Preibisch, T., 1997, A&A, 320, 525-539.
- Preibisch, T., Zinnecker, H., 2002, AJ, 123, 1623.
- Preibisch, T., 2003, A&A, 401, 543-555.
- Preibisch, T., Kim, Y., Favata, F., et al., 2005, ApJS, 160, 401.
- Preibisch, T., Feigelson, E., 2005, ApJS, 160, 390.
- Racine, R., 1968, AJ, 73, 233.
- Rieke, G., Lebosky, ., 1985, ApJ, 288, 618.
- Rieke, et al., 2004, ApJS, 154, 25-29.
- Romanov, M.M., et al., 2004, ApJ, 616, L151.
- Schmitt, J.H.M.M., Collura, A., Sciortino, S., Vaiana, G.S., Harnden, F.R., Rosner, R., 1990, ApJ, 365, 704.
- Siess, L., Dufour, E., Forestini, M., 2000, A&A, 358, 593.
- Skrutskie, M.F., Cutri R.M., Stiening R., et al., 2006, AJ, 131, 1163.
- Stelzer, B., Neuhauser, R., 2001, A&A, 377, 538.

- Stern, R.A., Schmitt, J.H.M.M., Pye, J.P., et al., 1994, *ApJ*, 427, 808.
- Straizys, V., Černis, K., Bartašiūtė, S., 1996, *Baltic Astron.*, 5, 125
- Straizys, V., Černis, K., Bartašiūtė, S., 2003, *A&A*, 405, 585.
- Strom, S. E., Grasdalen, G. L., Strom, K. M. 1974, *ApJ*, 191, 111.
- Telleschi, A., Gudel, M., Briggs, K.R., Audard, M., Palla, F., 2007, *A&A*, 468, 425.
- Testi, L., Sargent, A., 1998, *ApJ*, 508, L91-L94.
- Testi, L., Sargent, A., Olmi L., Onella J., 2000, *ApJ*, 540, L53-L56.
- Young, M. H., et al., 2003, *A&A*, 408, 581-599.
- Willing, B.A., 1989, *Publ. Astron. Soc. Pacific*, 101, 229.
- Willing B.A., Meyer, M.R., Greene, T.P., Mikhail, A., Carlson, G., 2004, *AJ*, 127, 1131.
- Winston, E., Megeath, S.T., Wolk, S.J., Muzerolle, J., Gutermuth, R., Hora, J.L., Allen, L.E., Spitzbart, B., Myers, P., Fazio, G.G., 2007, *ApJ*, 669, 493.
- Winston, E., Megeath, S.T., Wolk, S.J., Muzerolle, J., Gutermuth, R., Hora, J.L., Allen, L.E., Hernandez, J., Covey, K., Spitzbart, B., Myers, P., Fazio, G.G., 2009, *AJ*, 137, 447.
- Wolk, S. J., Spitzbart, B. D., Bourke, T. L., Alves, J., 2006, *AJ*, 132, 1100-1125.
- Wolk, S. J., et al., 2008, *AJ*, 135, 693.
- Zhang, C. Y., Laurejs, R. J., Clark, F. O., Wesselius, P. R. 1988, *A&A*, 199, 170.

Table 1. NGC 1333: *Chandra* X-ray Source Photometry

<i>Chandra</i> ID	RA (2000)	Dec (2000)	Raw CNT	Net ^a CNT	N_H 10^{22}cm^{-2}	kT keV	Abs. Flux $\log([\text{erg cm}^{-2} \text{s}^{-1}])$	Tot. UnAbs. Flux	χ^2
1	3:29:03.03	31:15:17.09	47	40.2	$4.18 \pm \dots$	$12.09 \pm \dots$	-14.06	-13.72	1.01
2	3:28:52.16	31:15:47.75	36	29.5	0.10 ± 0.14	0.96 ± 0.09	-14.73	-14.58	0.80
3	3:28:59.32	31:15:49.56	1552	1544	1.46 ± 0.08	2.39 ± 0.16	-12.79	-12.36	2.23
4	3:29:02.91	31:16:01.63	273	268	0.00 ± 0.00	1.00 ± 0.04	-13.76	-13.76	1.00
5	3:29:02.18	31:16:12.15	71	65.7	0.02 ± 0.07	0.84 ± 0.04	-14.40	-14.36	0.72
6	3:29:21.15	31:16:17.47	62	50.2	$18.07 \pm \dots$	\dots	-13.76	-13.21	1.24
7	3:29:03.50	31:16:18.34	52	47.4	2.94 ± 0.77	2.63 ± 1.14	-14.18	-13.66	0.77
8	3:29:16.72	31:16:19.45	408	400	0.00 ± 0.02	1.08 ± 0.03	-13.58	-13.58	1.32
9	3:28:56.99	31:16:22.98	168	162	0.41 ± 0.09	2.37 ± 0.39	-13.88	-13.64	1.14
10	3:28:55.19	31:16:25.46	116	110	0.28 ± 0.12	5.17 ± 0.01	-13.95	-13.81	0.99
11	3:28:55.09	31:16:29.29	171	165	0.81 ± 0.13	2.37 ± 0.41	-13.82	-13.48	1.03
12	3:28:59.26	31:16:30.94	12	6.77	0.00 ± 0.01	1.65 ± 0.00	-15.22	-15.22	0.63
13	3:28:46.22	31:16:39.45	723	715	0.11 ± 0.03	1.04 ± 0.03	-13.35	-13.19	1.52
14	3:29:05.82	31:16:40.23	455	451	1.36 ± 0.15	3.40 ± 0.56	-13.28	-12.95	1.55
16	3:28:54.65	31:16:51.66	492	486	0.52 ± 0.11	2.90 ± 0.65	-13.36	-13.12	1.58
17	3:28:47.86	31:16:56.03	97	89.7	0.18 ± 0.08	2.32 ± 0.01	-14.15	-13.99	1.14
18	3:29:18.14	31:17:05.51	19	14.5	$1.85 \pm \dots$	\dots	-14.53	-14.34	0.67
19	3:28:43.38	31:17:02.72	12	4.55	$30.62 \pm \dots$	\dots	-14.75	-14.05	0.74
20	3:29:04.11	31:17:08.25	134	129	0.07 ± 0.06	1.04 ± 0.06	-14.13	-14.02	0.95
22	3:29:11.34	31:17:18.47	183	177	0.00 ± 0.01	2.00 ± 0.19	-13.87	-13.87	1.19
23	3:28:43.31	31:17:33.49	309	301	2.78 ± 0.26	3.95 ± 0.61	-13.32	-12.91	1.68
25	3:28:36.96	31:17:36.32	900	875	0.29 ± 0.04	2.04 ± 0.14	-13.15	-12.93	2.33
26	3:28:43.58	31:17:37.27	536	528	0.35 ± 0.07	3.73 ± 0.54	-13.30	-13.13	1.89
27	3:29:13.64	31:17:44.34	28	23.0	$1.49 \pm \dots$	$1.44 \pm \dots$	-14.70	-14.10	0.81
28	3:28:56.21	31:17:44.95	24	21.5	0.01 ± 0.16	1.01 ± 0.12	-14.86	-14.84	0.51
29	3:29:19.05	31:17:58.72	9	4.70	\dots	\dots	\dots	\dots	\dots
30	3:28:58.13	31:18:04.47	183	180	0.53 ± 0.12	1.00 ± 0.08	-14.02	-13.53	0.85
32	3:28:53.97	31:18:09.97	442	439	1.29 ± 0.15	2.19 ± 0.29	-13.37	-12.94	1.52
33	3:28:56.85	31:18:11.74	8	5.92	4.99 ± 0.44	1.89 ± 0.92	-14.98	-14.19	0.40
34	3:29:12.97	31:18:15.30	850	847	6.12 ± 0.34	3.03 ± 0.27	-12.82	-12.19	1.78
35	3:28:55.02	31:18:16.03	18	15.7	$0.18 \pm \dots$	\dots	-14.73	-14.66	0.50
36	3:28:51.06	31:18:18.82	154	152	0.17 ± 0.06	6.11 ± 0.00	-13.81	-13.72	0.95
37	3:29:20.43	31:18:35.08	138	132	2.07 ± 0.24	4.05 ± 0.05	-13.73	-13.37	1.20
38	3:29:29.27	31:18:35.77	1798	1782	0.44 ± 0.04	5.18 ± 0.55	-12.72	-12.56	4.88
39	3:28:56.67	31:18:36.47	284	281	0.75 ± 0.16	2.41 ± 0.55	-13.60	-13.28	1.23
40	3:29:03.43	31:18:40.02	25	22.6	0.00 ± 0.02	1.08 ± 0.09	-14.83	-14.83	0.50
41	3:29:15.65	31:18:52.65	54	51.6	17.52 ± 0.55	8.76 ± 1.22	-13.83	-13.20	0.72
42	3:29:23.22	31:19:02.19	13	8.00	0.00 ± 0.03	6.78 ± 0.00	-14.90	-14.90	0.61
43	3:28:56.15	31:19:09.15	16	14.4	8.75 ± 0.00	9.55 ± 0.00	-14.45	-13.98	0.43
44	3:29:22.17	31:19:23.56	23	18.0	$0.64 \pm \dots$	\dots	-14.51	-14.39	0.65
45	3:28:48.18	31:19:24.35	14	12.1	0.33 ± 0.10	$0.24 \pm \dots$	-15.06	-14.20	0.37
46	3:29:18.61	31:19:26.22	77	74.7	3.44 ± 0.55	5.09 ± 0.08	-13.88	-13.48	0.79
47	3:28:36.54	31:19:30.07	89	76.1	0.11 ± 0.12	0.86 ± 0.06	-14.28	-14.11	1.46
48	3:28:59.94	31:19:31.12	6	4.04	\dots	\dots	\dots	\dots	\dots
49	3:28:48.80	31:19:31.67	29	27.1	$1.34 \pm \dots$	$13.67 \pm \dots$	-14.26	-14.05	0.48

Table 1—Continued

<i>Chandra</i> ID	RA (2000)	Dec (2000)	Raw CNT	Net ^a CNT	N_H 10^{22} cm^{-2}	kT keV	Abs. Flux $\log([\text{erg cm}^{-2} \text{ s}^{-1}])$	Tot. UnAbs. Flux	χ^2
50	3:29:06.64	31:19:34.05	32	30.5	$1.82 \pm \dots$	\dots	-14.15	-13.95	0.50
51	3:28:57.73	31:19:48.84	630	627	0.24 ± 0.04	2.85 ± 0.28	-13.21	-13.05	1.66
52	3:28:57.45	31:19:51.09	166	163	0.70 ± 0.12	0.77 ± 0.06	-14.01	-13.29	0.79
53	3:28:51.22	31:19:55.37	1297	1294	0.32 ± 0.03	1.72 ± 0.09	-13.05	-12.79	1.60
54	3:28:55.08	31:19:55.88	7	5.30	\dots	\dots	\dots	\dots	\dots
56	3:29:12.83	31:20:08.69	18	16.3	0.87 ± 0.28	0.34 ± 0.05	-15.01	-13.68	0.37
57	3:29:09.28	31:20:14.38	10	8.42	4.91 ± 2.26	2.32 ± 0.81	-14.78	-14.10	0.34
58	3:28:39.25	31:20:16.88	15	7.52	$3.31 \pm \dots$	\dots	-14.55	-14.30	0.82
59	3:28:54.11	31:20:20.41	10	7.93	\dots	\dots	\dots	\dots	\dots
60	3:29:08.34	31:20:20.27	10	8.71	$1.88 \pm \dots$	$0.71 \pm \dots$	-15.13	-13.84	0.26
61	3:28:46.89	31:20:28.55	23	18.9	0.00 ± 0.02	0.98 ± 0.12	-14.86	-14.86	0.66
62	3:29:04.58	31:20:29.48	16	13.7	$0.38 \pm \dots$	\dots	-14.71	-14.61	0.45
63	3:28:44.99	31:20:33.59	10	6.19	\dots	\dots	\dots	\dots	\dots
64	3:29:27.08	31:20:31.71	12	6.89	\dots	\dots	\dots	\dots	\dots
65	3:28:39.62	31:20:34.15	16	9.21	$0.00 \pm \dots$	\dots	-14.93	-14.93	0.74
66	3:28:51.31	31:20:38.87	17	14.6	3.51 ± 0.00	9.55 ± 0.00	-14.51	-14.19	0.53
67	3:29:04.95	31:20:39.19	9	7.25	\dots	\dots	\dots	\dots	\dots
68	3:29:00.41	31:20:46.42	32	29.7	$0.34 \pm \dots$	$1.14 \pm \dots$	-14.79	-14.45	0.52
69	3:28:45.86	31:20:49.28	8	4.25	$100. \pm \dots$	\dots	-14.84	-13.49	0.45
70	3:28:45.45	31:20:51.01	71	67.5	1.24 ± 0.29	$\dots \pm 0.00$	-13.86	-13.70	0.80
71	3:29:16.60	31:21:03.56	16	13.8	0.96 ± 0.46	1.72 ± 0.67	-14.94	-14.50	0.46
72	3:29:29.78	31:21:03.39	89	81.6	0.09 ± 0.08	2.10 ± 0.28	-14.21	-14.11	1.08
73	3:29:19.08	31:21:07.18	66	63.9	$0.96 \pm \dots$	$13.95 \pm \dots$	-14.06	-13.88	0.70
74	3:29:00.18	31:21:10.22	17	14.8	2.38 ± 0.65	0.82 ± 0.25	-14.87	-13.64	0.42
75	3:29:24.16	31:21:10.32	38	30.3	$3.30 \pm \dots$	\dots	-14.17	-13.89	0.93
76	3:29:21.56	31:21:11.27	206	200	0.17 ± 0.06	1.28 ± 0.10	-13.91	-13.71	1.11
77	3:29:00.53	31:21:26.89	10	8.44	\dots	\dots	\dots	\dots	\dots
78	3:29:11.90	31:21:27.92	38	36.2	2.55 ± 0.67	3.88 ± 1.99	-14.10	-13.70	0.58
79	3:29:09.16	31:21:44.63	19	16.8	\dots	\dots	\dots	\dots	\dots
80	3:28:59.57	31:21:47.43	51	48.8	0.47 ± 0.16	2.24 ± 0.45	-14.42	-14.15	0.64
81	3:29:03.88	31:21:49.44	1051	1048	0.54 ± 0.04	2.40 ± 0.15	-13.09	-12.81	1.79
82	3:29:07.75	31:21:56.91	56	54.5	\dots	\dots	\dots	\dots	\dots
83	3:28:47.93	31:21:57.56	43	38.7	4.16 ± 1.12	\dots	-14.03	-13.75	0.88
84	3:29:10.40	31:21:59.85	3796	3792	1.03 ± 0.04	1.97 ± 0.07	-12.50	-12.08	2.14
85	3:29:00.72	31:22:01.54	67	64.8	$1.24 \pm \dots$	$1.44 \pm \dots$	-14.31	-13.75	0.66
86	3:29:10.56	31:22:01.49	879	875	1.01 ± 0.08	2.25 ± 0.16	-13.11	-12.73	2.58
87	3:29:14.07	31:22:14.65	38	35.1	$2.03 \pm \dots$	\dots	-14.22	-14.00	0.66
88	3:29:02.79	31:22:17.84	9	6.81	$1.92 \pm \dots$	$0.90 \pm \dots$	-15.26	-14.23	0.41
89	3:28:58.43	31:22:18.19	107	104	21.58 ± 2.09	$9.05 \pm \dots$	-13.50	-12.81	0.95
90	3:28:43.44	31:22:21.58	14	8.06	$0.00 \pm \dots$	\dots	-14.87	-14.87	0.68
91	3:28:45.52	31:22:28.37	13	9.04	\dots	\dots	\dots	\dots	\dots
92	3:28:56.27	31:22:28.01	21	18.7	$0.96 \pm \dots$	$1.83 \pm \dots$	-14.76	-14.33	0.43
93	3:29:29.55	31:22:28.79	15	7.41	$0.00 \pm \dots$	\dots	-14.84	-14.84	0.81
94	3:29:10.81	31:22:30.75	40	37.4	$1.19 \pm \dots$	$0.71 \pm \dots$	-14.70	-13.65	0.58
95	3:29:14.45	31:22:36.91	38	35.3	\dots	\dots	\dots	\dots	\dots

Table 1—Continued

<i>Chandra</i> ID	RA (2000)	Dec (2000)	Raw CNT	Net ^a CNT	N_H 10^{22} cm^{-2}	kT keV	Abs. Flux $\log([\text{erg cm}^{-2} \text{ s}^{-1}])$	Tot. UnAbs. Flux	χ^2
96	3:29:03.15	31:22:38.27	25	22.9	0.74 ± 0.35	...	-14.47	-14.35	0.53
97	3:28:56.59	31:22:41.08	8	5.68
98	3:29:17.67	31:22:45.60	6397	6391	0.28 ± 0.01	2.46 ± 0.08	-12.32	-12.12	2.40
99	3:28:52.18	31:22:46.02	525	520	0.13 ± 0.03	2.44 ± 0.17	-13.42	-13.30	1.58
100	3:29:07.97	31:22:52.29	299	297	1.34 ± 0.39	2.21 ± 0.78	-13.47	-13.03	1.05
101	3:29:13.13	31:22:53.27	56	53.7	1.10 ± 0.27	2.41 ± 0.66	-14.30	-13.92	0.65
102	3:28:45.56	31:22:55.01	27	22.7	$3.69 \pm$	-14.26	-14.00	0.77
103	3:29:09.14	31:23:06.23	18	15.5	1.80 ± 0.99	1.19 ± 0.62	-14.84	-14.08	0.49
104	3:28:36.96	31:23:12.58	864	851.	0.20 ± 0.03	1.35 ± 0.05	-13.25	-13.03	1.94
105	3:28:59.08	31:23:21.18	12	7.78	0.00 ± 0.04	$0.19 \pm$...	-14.94	-14.94	0.69
106	3:29:18.73	31:23:26.27	679	670	0.20 ± 0.04	1.03 ± 0.03	-13.45	-13.19	1.62
107	3:29:23.50	31:23:31.69	1033	1025	0.29 ± 0.03	2.24 ± 0.10	-13.11	-12.90	2.29
108	3:28:51.01	31:23:48.29	316	309	1.59 ± 0.19	2.58 ± 0.41	-13.46	-13.04	1.84
109	3:29:16.62	31:23:50.36	264	255	0.66 ± 0.14	2.69 ± 0.62	-13.64	-13.36	1.60
110	3:28:47.65	31:24:06.54	58	51.9	0.89 ± 0.20	2.22 ± 0.07	-14.32	-13.96	0.92
111	3:29:20.07	31:24:08.29	75	67.5	2.91 ± 0.49	2.56 ± 0.56	-13.99	-13.46	1.07
112	3:29:22.05	31:24:15.78	223	216	0.00 ± 0.05	1.05 ± 0.04	-13.83	-13.83	1.12
113	3:29:13.49	31:24:41.09	53	46.0	9.96 ± 2.60	...	-13.88	-13.47	1.04
114	3:29:18.63	31:24:41.85	12	5.03	$100. \pm$	-14.66	-13.31	0.66
116	3:29:19.78	31:24:58.24	136	122	0.74 ± 0.20	0.95 ± 0.12	-14.14	-13.53	1.37
117	3:29:19.13	31:25:00.66	19	5.38	$0.00 \pm$...	$2.01 \pm$...	-15.16	-15.16	1.09
118	3:28:42.22	31:24:59.12	19	7.26
119	3:28:47.61	31:25:19.13	17	4.89	0.00 ± 0.02	0.15 ± 0.02	-14.45	-14.45	1.09
120	3:28:59.63	31:25:42.69	32	20.9	12.07 ± 0.42	2.92 ± 1.23	-14.26	-13.45	1.27
121	3:28:49.40	31:26:17.29	20	7.49	$0.00 \pm$	-14.96	-14.96	1.26
122	3:28:59.31	31:26:39.07	68	56.4	1.45 ± 0.39	...	-13.97	-13.79	1.44
123	3:28:57.10	31:15:02.74	43	24.8	0.19 ± 0.22	...	-14.32	-14.26	1.35
124	3:28:49.09	31:15:18.56	24	9.96	0.00 ± 0.01	...	-14.74	-14.74	1.12
125	3:29:08.71	31:15:20.34	18	13.0
126	3:29:17.65	31:15:45.63	23	9.23	0.00 ± 0.01	5.04 ± 0.00	-14.78	-14.78	1.12
127	3:29:07.15	31:15:57.90	11	7.85
128	3:28:51.04	31:16:32.44	16	9.33	0.00 ± 0.08	3.25 ± 0.01	-14.99	-14.99	0.79
129	3:28:55.29	31:17:35.78	14	11.5	1.39 ± 0.32	0.23 ± 0.02	-15.27	-12.94	0.41
130	3:29:24.34	31:18:05.79	33	26.5	2.60 ± 0.00	...	-14.29	-14.06	0.92
131	3:28:46.15	31:18:30.65	24	17.2	$0.00 \pm$	-14.67	-14.67	0.89
132	3:29:30.46	31:19:02.92	35	19.5	0.00 ± 0.02	6.80 ± 0.00	-14.54	-14.54	1.22
133	3:29:17.05	31:19:10.16	9	6.63
134	3:29:24.68	31:20:23.81	24	17.9	$2.03 \pm$	-14.34	-14.14	0.67
135	3:29:23.22	31:20:31.39	20	15.8	0.34 ± 0.25	0.84 ± 0.09	-14.99	-14.58	0.59
136	3:29:24.88	31:20:52.08	57	50.6	$1.60 \pm$...	$2.24 \pm$...	-14.25	-13.79	0.96
137	3:28:44.11	31:20:53.45	13	10.0	$0.00 \pm$...	$1.29 \pm$...	-14.96	-14.96	0.50
138	3:29:04.08	31:20:53.45	12	10.3	17.13 ± 0.08	1.97 ± 0.82	-14.70	-13.55	0.39
139	3:28:35.09	31:21:11.96	37	26.4	5.07 ± 1.88	2.93 ± 1.64	-14.28	-13.69	1.18
140	3:28:31.91	31:21:21.26	70	50.9	2.79 ± 0.74	...	-13.90	-13.67	1.54
141	3:29:31.69	31:21:24.81	34	20.4	0.22 ± 0.25	...	-14.48	-14.41	1.17

Table 1—Continued

<i>Chandra</i> ID	RA (2000)	Dec (2000)	Raw CNT	Net ^a CNT	N_H 10^{22} cm^{-2}	kT keV	Abs. Flux $\log([\text{erg cm}^{-2} \text{ s}^{-1}])$	Tot. UnAbs. Flux	χ^2
142	3:28:42.26	31:22:18.65	23	15.6	$1.68 \pm \dots$	$11.17 \pm \dots$	-14.52	-14.29	0.85
143	3:29:24.84	31:24:06.69	30	22.9	0.00 ± 0.02	0.94 ± 0.06	-14.74	-14.74	0.85
144	3:28:49.51	31:24:15.76	19	11.0	$2.82 \pm \dots$	\dots	-14.49	-14.22	0.86
145	3:29:04.84	31:24:34.84	12	9.85	\dots	\dots	\dots	\dots	\dots
146	3:28:59.83	31:24:41.95	21	17.4	3.09 ± 0.98	3.03 ± 1.27	-14.56	-14.07	0.66
147	3:29:05.76	31:24:54.79	8	5.01	10.73 ± 0.10	2.30 ± 1.02	-14.75	-13.85	0.60
148	3:29:23.73	31:25:09.14	49	28.4	$0.00 \pm \dots$	$6.83 \pm \dots$	-14.38	-14.38	1.53
149	3:29:04.21	31:25:15.74	48	43.2	0.76 ± 0.28	2.54 ± 1.09	-14.10	-13.79	0.80
150	3:28:51.50	31:25:14.45	29	16.3	1.28 ± 0.17	5.96 ± 0.23	-14.49	-14.24	1.25000
151	3:28:48.65	31:25:23.98	37	24.3	0.90 ± 0.50	\dots	-14.33	-14.19	1.05
152	3:29:02.99	31:25:45.64	12	1.26	\dots	\dots	\dots	\dots	\dots
153	3:29:07.04	31:27:02.29	25	15.2	$4.49 \pm \dots$	\dots	-14.38	-14.06	1.07
155	3:28:53.66	31:15:38.58	18	10.4	$4.27 \pm \dots$	$1.54 \pm \dots$	-14.75	-13.89	0.80
156	3:28:48.58	31:24:47.53	29	16.2	0.00 ± 0.02	$0.18 \pm \dots$	-14.64	-14.64	1.04
161	3:29:00.34	31:13:39.51	1019	997	$0.32 \pm \dots$	$2.28 \pm \dots$	-13.10	-12.88	2.70
162	3:28:55.16	31:14:16.53	38	21.2	$1.18 \pm \dots$	$10.57 \pm \dots$	-14.32	-14.12	1.26
163	3:28:57.24	31:14:19.94	8015	7996	0.04 ± 0.01	1.06 ± 0.01	-12.25	-12.18	3.27
164	3:29:25.22	31:15:27.19	38	25.2	0.00 ± 0.04	\dots	-14.37	-14.37	1.11
165	3:29:21.85	31:15:37.43	103	91.0	3.38 ± 0.55	3.21 ± 0.83	-13.82	-13.33	1.37
166	3:29:28.17	31:16:29.52	316	302	0.06 ± 0.04	1.12 ± 0.03	-13.72	-13.62	1.72
167	3:29:39.33	31:16:31.03	58	20.6	$1.13 \pm \dots$	\dots	-14.18	-14.02	2.02
168	3:29:26.40	31:16:56.30	32	18.2	$10.94 \pm \dots$	\dots	-14.16	-13.69	1.19
169	3:29:34.32	31:17:44.45	1506	1484	0.04 ± 0.02	2.46 ± 0.17	-12.90	-12.85	3.47
170	3:29:33.73	31:20:27.48	28	12.9	$3.54 \pm \dots$	\dots	-14.36	-14.10	1.11
171	3:29:46.37	31:20:40.19	81	59.4	0.18 ± 0.15	0.86 ± 0.05	-14.06	-13.80	1.65
173	3:28:29.71	31:25:11.78	91	45.4	0.14 ± 0.18	\dots	-14.00	-13.95	2.01
174	3:28:37.84	31:25:27.26	72	39.7	1.75 ± 0.54	\dots	-14.00	-13.81	1.98
175	3:29:25.99	31:26:41.57	1458	1425	0.28 ± 0.03	4.54 ± 0.28	-12.83	-12.69	3.21
176	3:29:26.81	31:26:48.34	4046	4014	0.15 ± 0.01	1.34 ± 0.02	-12.57	-12.39	3.33
177	3:29:19.49	31:27:05.59	24	4.74	$0.00 \pm \dots$	\dots	-14.75	-14.75	1.35
178	3:29:24.94	31:27:45.84	56	11.3	0.00 ± 0.01	\dots	-14.34	-14.34	1.84
179	3:29:04.73	31:11:35.06	35	26.0	\dots	\dots	\dots	\dots	\dots
180	3:29:08.78	31:13:15.71	35	13.4	$2.47 \pm \dots$	\dots	-14.11	-13.88	1.66
181	3:29:25.89	31:13:44.37	86	59.4	$1.05 \pm \dots$	$11.63 \pm \dots$	-13.94	-13.7500	1.85
182	3:29:25.71	31:13:57.23	82	52.9	0.75 ± 0.25	\dots	-13.98	-13.85	1.86
183	3:29:32.87	31:27:13.52	86	39.3	0.00 ± 0.00	3.32 ± 0.00	-14.15	-14.15	1.91
184	3:28:50.46	31:27:55.36	85	63.7	1.02 ± 0.28	5.02 ± 0.01	-14.06	-13.81	1.75
185	3:29:21.99	31:28:31.76	62	26.2	$1.46 \pm \dots$	$11.55 \pm \dots$	-14.08	-13.8700	1.79
186	3:28:58.49	31:11:41.17	34	22.2	\dots	\dots	\dots	\dots	\dots
187	3:29:37.54	31:20:41.53	26	4.64	3.77 ± 0.08	6.28 ± 0.35	-14.53	-14.15	1.38
188	3:29:30.55	31:27:27.10	78	32.3	0.00 ± 0.01	8.90 ± 0.37	-14.15	-14.15	1.76
189	3:29:31.57	31:14:07.07	42	13.5	2.85 ± 1.17	\dots	-14.27	-14.04	1.69
190	3:29:41.29	31:14:06.19	82	42.6	0.00 ± 0.01	\dots	-14.12	-14.12	2.00
191	3:29:43.95	31:14:06.71	80	51.2	0.00 ± 0.01	\dots	-14.09	-14.09	1.82
192	3:29:44.02	31:15:10.42	80	28.5	0.00 ± 0.11	\dots	-14.15	-14.15	2.20

^aNet Counts: background subtracted and aperture corrected from raw counts.^bAbs. Flux: Absorbed flux. Tot. UnAbs. Flux: Total unabsorbed flux.

Table 2. NGC 1333: Coordinates & IR Photometry of X-ray sources

<i>Ch.</i> ID	RA X-ray	Dec (2000)	RA Infrared	Dec (2000) ^a	Sep. ^b "	<i>J</i> mag	<i>H</i> mag	<i>K</i> mag	3.6 μ m mag	4.5 μ m mag	5.8 μ m mag	8.0 μ m mag	24 μ m mag
1	3:29:03.03	31:15:17.09	3:29:02.97	31:15:16.73	0.364	13.356 \pm 0.112	11.9689 \pm 0.069	11.524 \pm 0.025	11.475 \pm 0.052	...
2	3:28:52.16	31:15:47.75	3:28:52.13	31:15:47.18	0.157	13.161 \pm 0.021	12.469 \pm 0.026	12.029 \pm 0.022	11.356 \pm 0.005	11.112 \pm 0.006	10.804 \pm 0.013	10.001 \pm 0.001	7.8350 \pm 0.033
3	3:28:59.32	31:15:49.55	3:28:59.30	31:15:48.52	0.198	16.490 \pm 0.16	12.528 \pm 0.027	10.437 \pm 0.019	8.5941 \pm 0.002	8.0706 \pm 0.003	7.4837 \pm 0.003	6.4121 \pm 0.002	2.4270 \pm 0.032
4	3:29:02.91	31:16:01.64	3:29:02.89	31:16:01.03	0.268	12.838 \pm 0.019	12.177 \pm 0.033	11.943 \pm 0.028	11.541 \pm 0.043	...	10.843 \pm 0.115
5	3:29:02.18	31:16:12.15	3:29:02.16	31:16:11.43	0.143	14.526 \pm 0.030	13.865 \pm 0.040	13.567 \pm 0.034	13.279 \pm 0.034	12.692 \pm 0.057
8	3:29:16.72	31:16:19.45	3:29:16.67	31:16:18.29	0.113	11.443 \pm 0.021	10.748 \pm 0.028	10.431 \pm 0.020	10.166 \pm 0.003	10.159 \pm 0.004	10.152 \pm 0.009	10.124 \pm 0.011	...
9	3:28:56.99	31:16:22.97	3:28:56.94	31:16:22.28	0.145	13.760 \pm 0.027	11.923 \pm 0.024	11.081 \pm 0.021	10.453 \pm 0.003	10.275 \pm 0.004	9.9456 \pm 0.008	8.8774 \pm 0.005	3.9040 \pm 0.031
10	3:28:55.19	31:16:25.46	3:28:55.14	31:16:24.73	0.273	13.010 \pm 0.038	11.656 \pm 0.054	10.927 \pm 0.022	9.6916 \pm 0.005	9.4149 \pm 0.005	8.7645 \pm 0.006	7.9788 \pm 0.003	...
11	3:28:55.09	31:16:29.29	3:28:55.05	31:16:28.74	0.200	13.581 \pm 0.024	11.705 \pm 0.026	10.676 \pm 0.046	9.0931 \pm 0.003	8.6282 \pm 0.003	8.1808 \pm 0.003	7.3751 \pm 0.002	3.9140 \pm 0.040
12	3:28:59.25	31:16:30.94	3:28:59.34	31:16:31.56	1.485	17.039 \pm 0.25	15.604 \pm 0.147	14.554 \pm 0.105	13.964 \pm 0.017	13.900 \pm 0.024	13.909 \pm 0.118
13	3:28:46.22	31:16:39.45	3:28:46.18	31:16:38.59	0.216	10.875 \pm 0.017	10.005 \pm 0.019	9.6900 \pm 0.018	9.3190 \pm 0.003	9.2269 \pm 0.003	8.8889 \pm 0.005	8.3018 \pm 0.004	6.8200 \pm 0.034
14	3:29:05.82	31:16:40.23	3:29:05.75	31:16:39.69	0.757	14.488 \pm 0.055	11.613 \pm 0.043	9.9310 \pm 0.026	8.4898 \pm 0.002	7.8564 \pm 0.003	7.2239 \pm 0.003	6.3857 \pm 0.001	3.7000 \pm 0.032
16	3:28:54.65	31:16:51.66	3:28:54.61	31:16:51.21	0.283	12.860 \pm 0.020	11.193 \pm 0.021	10.232 \pm 0.019	9.3516 \pm 0.003	8.9790 \pm 0.003	8.5442 \pm 0.005	7.6631 \pm 0.002	4.5890 \pm 0.032
17	3:28:47.86	31:16:56.03	3:28:47.82	31:16:55.21	0.288	12.940 \pm 0.021	11.759 \pm 0.023	10.909 \pm 0.019	9.8690 \pm 0.003	9.3871 \pm 0.003	9.0851 \pm 0.006	8.3665 \pm 0.003	5.5900 \pm 0.033
20	3:29:04.11	31:17:08.25	3:29:04.06	31:17:7.544	0.374	13.310 \pm 0.021	12.675 \pm 0.031	12.313 \pm 0.022	11.922 \pm 0.008	11.942 \pm 0.011	11.927 \pm 0.031	11.811 \pm 0.056	...
22	3:29:11.34	31:17:18.47	3:29:11.31	31:17:17.59	0.133	13.977 \pm 0.024	13.371 \pm 0.031	12.915 \pm 0.026	12.329 \pm 0.007	12.335 \pm 0.010	12.342 \pm 0.033	12.138 \pm 0.047	...
23	3:28:43.31	31:17:33.49	3:28:43.26	31:17:33.08	0.491	12.588 \pm 0.020	10.861 \pm 0.051	9.7470 \pm 0.036	7.7596 \pm 0.003	6.8910 \pm 0.002	5.9592 \pm 0.002	5.0015 \pm 0.001	1.6220 \pm 0.034
25	3:28:36.96	31:17:36.32	3:28:36.92	31:17:35.38	0.162	11.961 \pm 0.018	10.652 \pm 0.021	10.115 \pm 0.019	9.6910 \pm 0.003	9.6442 \pm 0.003	9.5634 \pm 0.007	9.5635 \pm 0.008	8.8840 \pm 0.036
26	3:28:43.58	31:17:37.26	3:28:43.55	31:17:36.46	0.046	12.219 \pm 0.035	10.963 \pm 0.023	10.138 \pm 0.019	8.9231 \pm 0.006	8.4845 \pm 0.006	...	6.3650 \pm 0.015	2.7200 \pm 0.038
27	3:29:13.64	31:17:44.33	3:29:13.61	31:17:43.49	0.184	16.441 \pm 0.129	14.250 \pm 0.050	13.028 \pm 0.032	12.010 \pm 0.007	11.855 \pm 0.008	11.707 \pm 0.030	11.676 \pm 0.064	...
28	3:28:56.20	31:17:44.94	3:28:56.22	31:17:45.73	0.834	13.478 \pm 0.023	12.647 \pm 0.027	12.170 \pm 0.025	11.697 \pm 0.006	11.618 \pm 0.007	11.550 \pm 0.020	11.538 \pm 0.038	...
30	3:28:58.13	31:18:04.46	3:28:58.09	31:18:03.82	0.284	12.809 \pm 0.020	11.707 \pm 0.023	11.345 \pm 0.021	11.084 \pm 0.005	11.080 \pm 0.006	10.953 \pm 0.016	10.831 \pm 0.019	...
32	3:28:53.97	31:18:09.97	3:28:53.92	31:18:09.28	0.241	14.819 \pm 0.058	12.266 \pm 0.035	10.878 \pm 0.022	9.9961 \pm 0.003	9.6645 \pm 0.004	9.2091 \pm 0.006	8.2847 \pm 0.003	4.8340 \pm 0.032
34	3:29:12.97	31:18:15.30	3:29:12.94	31:18:14.61	0.327	>18.598	>17.773	14.115 \pm 0.049	9.1850 \pm 0.003	7.5688 \pm 0.003	6.6501 \pm 0.002	5.7954 \pm 0.001	2.6050 \pm 0.035
35	3:28:55.01	31:18:16.03	3:28:54.97	31:18:15.33	0.155	>16.881	14.886 \pm 0.089	13.155 \pm 0.039	12.150 \pm 0.010	11.893 \pm 0.012	11.670 \pm 0.024	11.574 \pm 0.036	...
36	3:28:51.05	31:18:18.82	3:28:51.01	31:18:18.48	0.379	11.363 \pm 0.017	10.070 \pm 0.017	9.1840 \pm 0.018	8.3669 \pm 0.002	8.0023 \pm 0.002	7.5575 \pm 0.002	6.5665 \pm 0.001	3.5400 \pm 0.044
37	3:29:20.43	31:18:35.08	3:29:20.42	31:18:34.25	0.304	14.402 \pm 0.043	12.010 \pm 0.032	10.473 \pm 0.022	8.4437 \pm 0.002	7.9071 \pm 0.003	7.5122 \pm 0.002	6.6140 \pm 0.001	3.0740 \pm 0.032
38	3:29:29.27	31:18:35.76	3:29:29.25	31:18:34.77	0.208	12.587 \pm 0.021	11.374 \pm 0.027	10.963 \pm 0.020	10.605 \pm 0.004	10.660 \pm 0.005	10.594 \pm 0.012	10.071 \pm 0.010	4.7240 \pm 0.032
39	3:28:56.66	31:18:36.47	3:28:56.64	31:18:35.64	0.303	12.297 \pm 0.018	10.694 \pm 0.021	9.7020 \pm 0.019	8.7654 \pm 0.003	8.4191 \pm 0.003	8.2314 \pm 0.004	7.5448 \pm 0.003	3.6660 \pm 0.031
40	3:29:03.43	31:18:40.02	3:29:03.39	31:18:39.95	0.358	15.833 \pm 0.080	14.548 \pm 0.067	14.000 \pm 0.054	13.156 \pm 0.017	13.075 \pm 0.022	12.789 \pm 0.067	12.340 \pm 0.058	...
43	3:28:56.15	31:19:09.15	3:28:56.08	31:19:08.58	0.180	>19.530	>18.248	16.182 \pm 0.121	11.222 \pm 0.003	9.706 \pm 0.003	8.844 \pm 0.003	8.262 \pm 0.003	6.144 \pm 0.036
45	3:28:48.17	31:19:24.35	3:28:48.16	31:19:23.50	0.141	15.530 \pm 0.063	14.667 \pm 0.066	14.486 \pm 0.093	14.257 \pm 0.019	14.271 \pm 0.028
47	3:28:36.54	31:19:30.07	3:28:36.52	31:19:28.93	0.533	12.849 \pm 0.020	12.128 \pm 0.026	11.856 \pm 0.023	11.553 \pm 0.005	11.578 \pm 0.007	11.488 \pm 0.018	11.548 \pm 0.023	...
51	3:28:57.73	31:19:48.84	3:28:57.69	31:19:48.13	0.259	13.045 \pm 0.024	11.975 \pm 0.029	11.379 \pm 0.023	10.376 \pm 0.007	10.048 \pm 0.006	9.6557 \pm 0.009	8.6765 \pm 0.014	5.7300 \pm 0.032

Table 2—Continued

<i>Ch.</i> ID	RA X-ray	Dec (2000)	RA Infrared	Dec (2000) ^a	Sep. ^b "	<i>J</i> mag	<i>H</i> mag	<i>K</i> mag	3.6 μ m mag	4.5 μ m mag	5.8 μ m mag	8.0 μ m mag	24 μ m mag
52	3:28:57.45	31:19:51.09	3:28:57.41	31:19:50.56	0.413	12.131 \pm 0.036	11.055 \pm 0.044	10.664 \pm 0.037	10.246 \pm 0.004	10.225 \pm 0.006	10.064 \pm 0.012
53	3:28:51.22	31:19:55.36	3:28:51.19	31:19:54.89	0.270	11.716 \pm 0.017	10.493 \pm 0.021	9.8980 \pm 0.018	9.0558 \pm 0.002	8.7834 \pm 0.003	8.4014 \pm 0.004	7.3259 \pm 0.002	4.3190 \pm 0.032
56	3:29:12.82	31:20:08.69	3:29:12.79	31:20:7.706	0.193	14.676 \pm 0.030	13.781 \pm 0.035	13.294 \pm 0.033	12.854 \pm 0.012	12.793 \pm 0.012	12.705 \pm 0.098	12.707 \pm 0.093	...
60	3:29:08.35	31:20:20.27	3:29:08.32	31:20:20.34	0.199	14.681 \pm 0.032	12.904 \pm 0.028	12.011 \pm 0.020	11.268 \pm 0.005	11.161 \pm 0.005	11.035 \pm 0.017	10.991 \pm 0.026	...
61	3:28:46.89	31:20:28.54	3:28:46.87	31:20:27.78	0.227	14.809 \pm 0.038	14.246 \pm 0.052	13.798 \pm 0.055	13.492 \pm 0.013	13.531 \pm 0.017	13.506 \pm 0.072	13.357 \pm 0.13	...
62	3:29:04.58	31:20:29.47	3:29:04.62	31:20:28.91	0.507	>16.715	15.464 \pm 0.128	13.746 \pm 0.051	12.496 \pm 0.009	12.344 \pm 0.013	11.762 \pm 0.086	11.848 \pm 0.062	...
67	3:29:04.95	31:20:39.19	3:29:04.94	31:20:38.55	0.461	>15.575	14.601 \pm 0.140	12.975 \pm 0.066	11.210 \pm 0.009	10.489 \pm 0.006	9.7651 \pm 0.012	8.7860 \pm 0.007	4.7170 \pm 0.034
68	3:29:00.41	31:20:46.42	3:29:00.37	31:20:45.67	0.437	13.560 \pm 0.022	12.371 \pm 0.030	11.801 \pm 0.022	11.327 \pm 0.010	11.298 \pm 0.017	11.412 \pm 0.072	11.365 \pm 0.090	...
71	3:29:16.60	31:21:03.56	3:29:16.55	31:21:02.50	0.271	14.983 \pm 0.041	13.309 \pm 0.033	12.428 \pm 0.022	11.740 \pm 0.006	11.684 \pm 0.007	11.502 \pm 0.034	11.657 \pm 0.041	...
72	3:29:29.77	31:21:03.39	3:29:29.78	31:21:02.70	0.673	12.649 \pm 0.021	11.621 \pm 0.027	11.165 \pm 0.018	10.643 \pm 0.003	10.481 \pm 0.005	10.045 \pm 0.009	8.9783 \pm 0.005	6.0800 \pm 0.032
74	3:29:00.18	31:21:10.22	3:29:00.15	31:21:09.21	0.207	16.466 \pm 0.150	14.589 \pm 0.071	13.349 \pm 0.041	12.077 \pm 0.010	11.653 \pm 0.012	11.385 \pm 0.051	10.537 \pm 0.040	7.0770 \pm 0.042
76	3:29:21.56	31:21:11.27	3:29:21.55	31:21:10.47	0.222	12.393 \pm 0.019	11.723 \pm 0.031	11.372 \pm 0.020	10.929 \pm 0.004	10.692 \pm 0.005	10.367 \pm 0.012	9.7390 \pm 0.012	6.6490 \pm 0.032
78	3:29:11.90	31:21:27.92	3:29:11.88	31:21:27.13	0.262	>17.217	15.699 \pm 0.115	12.823 \pm 0.026	10.535 \pm 0.008	9.7033 \pm 0.005	9.0601 \pm 0.039	8.2793 \pm 0.068	...
79	3:29:09.16	31:21:44.63	3:29:09.15	31:21:44.56	0.761	>14.477	14.807 \pm 0.166	12.974 \pm 0.050	...	10.845 \pm 0.269
80	3:28:59.57	31:21:47.43	3:28:59.54	31:21:46.78	0.263	12.613 \pm 0.020	11.260 \pm 0.023	10.301 \pm 0.019	8.8253 \pm 0.002	8.4531 \pm 0.003	8.2146 \pm 0.004	7.4483 \pm 0.003	4.6670 \pm 0.031
81	3:29:03.88	31:21:49.44	3:29:03.86	31:21:48.71	0.243	11.536 \pm 0.027	10.138 \pm 0.031	9.2170 \pm 0.020	7.9393 \pm 0.001	7.6042 \pm 0.002	7.2056 \pm 0.004	6.3528 \pm 0.002	3.4630 \pm 0.034
82	3:29:07.75	31:21:56.91	3:29:07.74	31:21:57.52	0.634	>15.273	13.802 \pm 0.086	10.428 \pm 0.041	6.5950 \pm 0.005	5.1546 \pm 0.002	4.1675 \pm 0.005	3.6548 \pm 0.026	...
84	3:29:10.40	31:21:59.85	3:29:10.37	31:21:59.15	0.234	9.3680 \pm 0.027	7.9870 \pm 0.027	7.1730 \pm 0.017	6.6275 \pm 0.010	6.5693 \pm 0.011	6.0485 \pm 0.095
85	3:29:00.72	31:22:01.54	3:29:00.69	31:22:00.82	0.226	16.236 \pm 0.103	13.293 \pm 0.042	11.764 \pm 0.025	10.768 \pm 0.005	10.626 \pm 0.005	10.430 \pm 0.013	10.376 \pm 0.012	...
88	3:29:02.79	31:22:17.84	3:29:02.79	31:22:17.28	0.485	16.929 \pm 0.175	14.798 \pm 0.067	13.323 \pm 0.030	12.115 \pm 0.013	11.604 \pm 0.011	11.129 \pm 0.025	10.455 \pm 0.034	...
89	3:28:58.43	31:22:18.19	3:28:58.42	31:22:17.53	0.331	>18.417	14.805 \pm 0.086	11.849 \pm 0.025	9.6202 \pm 0.003	8.3179 \pm 0.003	7.2048 \pm 0.003	6.2872 \pm 0.001	2.2730 \pm 0.032
92	3:28:56.27	31:22:28.01	3:28:56.30	31:22:27.92	0.219	15.840 \pm 0.093	13.163 \pm 0.041	11.844 \pm 0.026	10.545 \pm 0.004	9.9718 \pm 0.004	9.2624 \pm 0.006	8.2785 \pm 0.003	4.7390 \pm 0.031
94	3:29:10.81	31:22:30.74	3:29:10.79	31:22:30.13	0.329	14.896 \pm 0.033	13.672 \pm 0.033	12.928 \pm 0.026	12.175 \pm 0.141	12.033 \pm 0.114
95	3:29:14.45	31:22:36.91	3:29:14.43	31:22:36.25	0.112	14.606 \pm 0.027	13.530 \pm 0.025	13.035 \pm 0.022	12.495 \pm 0.010	12.436 \pm 0.011	12.334 \pm 0.104	12.490 \pm 0.461	...
96	3:29:03.16	31:22:38.26	3:29:03.13	31:22:38.16	0.621	13.724 \pm 0.026	12.367 \pm 0.033	11.323 \pm 0.020	10.232 \pm 0.003	9.7583 \pm 0.004	9.2982 \pm 0.006	8.3102 \pm 0.005	4.9280 \pm 0.033
98	3:29:17.66	31:22:45.60	3:29:17.66	31:22:45.13	0.329	9.9730 \pm 0.019	8.9150 \pm 0.028	8.3240 \pm 0.020	7.2120 \pm 0.002	6.8422 \pm 0.002	6.2938 \pm 0.002	5.5634 \pm 0.001	2.8620 \pm 0.034
99	3:28:52.18	31:22:46.02	3:28:52.16	31:22:45.30	0.302	11.982 \pm 0.017	11.013 \pm 0.023	10.562 \pm 0.019	10.041 \pm 0.003	9.8584 \pm 0.003	9.5509 \pm 0.007	8.8180 \pm 0.004	6.3320 \pm 0.031
100	3:29:07.97	31:22:52.28	3:29:07.94	31:22:51.58	0.382	13.002 \pm 0.026	11.178 \pm 0.030	10.193 \pm 0.020	8.8778 \pm 0.003	8.4185 \pm 0.003	7.9211 \pm 0.014	7.2925 \pm 0.053	4.9150 \pm 0.054
101	3:29:13.13	31:22:53.26	3:29:13.12	31:22:52.91	0.299	12.867 \pm 0.019	11.117 \pm 0.027	10.109 \pm 0.020	8.6901 \pm 0.002	8.3537 \pm 0.002	7.9037 \pm 0.003	7.3920 \pm 0.006	5.2310 \pm 0.032
103	3:29:09.14	31:23:06.23	3:29:09.08	31:23:05.66	0.314	14.649 \pm 0.040	12.944 \pm 0.037	11.892 \pm 0.028	10.542 \pm 0.023	10.123 \pm 0.028	8.9394 \pm 0.091
104	3:28:36.95	31:23:12.58	3:28:36.95	31:23:12.12	0.486	11.781 \pm 0.017	10.820 \pm 0.021	10.497 \pm 0.019	10.254 \pm 0.003	10.246 \pm 0.004	10.177 \pm 0.009	10.120 \pm 0.011	10.114 \pm 0.076
106	3:29:18.73	31:23:26.27	3:29:18.72	31:23:25.44	0.304	11.446 \pm 0.021	10.676 \pm 0.028	10.330 \pm 0.020	9.5210 \pm 0.003	9.0162 \pm 0.003	8.3515 \pm 0.004	7.0611 \pm 0.004	3.8170 \pm 0.032
107	3:29:23.50	31:23:31.69	3:29:23.49	31:23:30.98	0.311	12.845 \pm 0.024	11.761 \pm 0.032	11.356 \pm 0.022	11.018 \pm 0.004	11.035 \pm 0.006	10.944 \pm 0.018	10.956 \pm 0.060	...
108	3:28:51.01	31:23:48.29	3:28:50.97	31:23:47.92	0.495	14.659 \pm 0.036	12.380 \pm 0.027	11.243 \pm 0.021	10.499 \pm 0.003	10.388 \pm 0.004	10.211 \pm 0.010	10.152 \pm 0.011	...

Table 2—Continued

<i>Ch.</i> ID	RA X-ray (2000)	Dec	RA Infrared (2000) ^a	Dec	Sep. ^b "	<i>J</i> mag	<i>H</i> mag	<i>K</i> mag	3.6 μ m mag	4.5 μ m mag	5.8 μ m mag	8.0 μ m mag	24 μ m mag
109	3:29:16.62	31:23:50.36	3:29:16.59	31:23:49.53	0.189	13.254 \pm 0.021	11.842 \pm 0.032	11.181 \pm 0.022	10.227 \pm 0.003	9.7708 \pm 0.003	9.2065 \pm 0.013	8.4131 \pm 0.036	6.4020 \pm 0.041
110	3:28:47.64	31:24:06.54	3:28:47.64	31:24:06.15	0.104	14.199 \pm 0.036	12.605 \pm 0.032	11.660 \pm 0.023	10.380 \pm 0.003	10.051 \pm 0.004	9.7673 \pm 0.008	9.3022 \pm 0.006	6.5500 \pm 0.031
111	3:29:20.07	31:24:08.29	3:29:20.03	31:24:07.64	0.353	>17.158	14.700 \pm 0.075	12.042 \pm 0.028	9.8334 \pm 0.009	9.0300 \pm 0.004	8.2877 \pm 0.041	7.3315 \pm 0.084	3.2570 \pm 0.034
112	3:29:22.04	31:24:15.78	3:29:22.04	31:24:15.37	0.387	11.998 \pm 0.019	11.266 \pm 0.030	11.002 \pm 0.020	10.723 \pm 0.005	10.738 \pm 0.005	10.690 \pm 0.040	10.700 \pm 0.269	...
116	3:29:19.78	31:24:58.24	3:29:19.77	31:24:57.23	0.199	8.8330 \pm 0.011	8.5380 \pm 0.035	8.3510 \pm 0.017	8.1954 \pm 0.002	8.2062 \pm 0.002	8.1887 \pm 0.017	8.2250 \pm 0.091	...
123	3:28:57.10	31:15:02.74	3:28:57.06	31:15:02.89	0.285	>18.314	>15.778	14.055 \pm 0.072	11.946 \pm 0.006	11.202 \pm 0.006	10.853 \pm 0.017	10.824 \pm 0.017	...
128	3:28:51.04	31:16:32.44	3:28:51.05	31:16:32.46	0.922	13.292 \pm 0.021	12.516 \pm 0.026	12.121 \pm 0.026	11.600 \pm 0.005	11.401 \pm 0.006	11.073 \pm 0.015	10.328 \pm 0.013	8.1520 \pm 0.034
129	3:28:55.29	31:17:35.78	3:28:55.24	31:17:35.40	0.138	15.090 \pm 0.047	14.073 \pm 0.052	13.433 \pm 0.045	12.898 \pm 0.010	12.777 \pm 0.012	12.717 \pm 0.038	12.704 \pm 0.072	...
132	3:29:30.46	31:19:02.92	3:29:30.38	31:19:3.464	0.866	12.110 \pm 0.019	11.391 \pm 0.031	11.026 \pm 0.020	10.477 \pm 0.003	...	9.7336 \pm 0.007	8.9126 \pm 0.005	6.0720 \pm 0.032
135	3:29:23.22	31:20:31.39	3:29:23.14	31:20:30.34	1.129	12.396 \pm 0.019	11.654 \pm 0.030	11.229 \pm 0.022	10.410 \pm 0.003	10.120 \pm 0.004	9.8240 \pm 0.009	8.9831 \pm 0.008	5.9240 \pm 0.032
137	3:28:44.11	31:20:53.45	3:28:44.07	31:20:52.86	0.455	14.245 \pm 0.032	13.235 \pm 0.035	12.627 \pm 0.029	11.862 \pm 0.006	11.645 \pm 0.007	11.314 \pm 0.017	10.575 \pm 0.018	8.0430 \pm 0.033
143	3:29:24.84	31:24:06.69	3:29:24.83	31:24:06.28	0.255	14.433 \pm 0.030	13.766 \pm 0.036	13.383 \pm 0.039	12.938 \pm 0.012	12.962 \pm 0.017	12.708 \pm 0.188
148	3:29:23.73	31:25:09.14	3:29:23.69	31:25:09.55	0.919	14.039 \pm 0.026	12.945 \pm 0.033	12.374 \pm 0.026	11.837 \pm 0.018	11.805 \pm 0.017	11.243 \pm 0.174
149	3:29:04.21	31:25:15.74	3:29:04.17	31:25:15.15	0.387	13.654 \pm 0.026	11.809 \pm 0.029	10.883 \pm 0.024	10.150 \pm 0.003	10.092 \pm 0.004	9.9521 \pm 0.010	9.9195 \pm 0.025	...
152	3:29:02.99	31:25:45.64	3:29:03.20	31:25:45.32	0.367	15.663 \pm 0.029	14.621 \pm 0.039	13.975 \pm 0.029	13.222 \pm 0.008	12.642 \pm 0.008	12.243 \pm 0.028	11.559 \pm 0.049	7.335 \pm 0.093
161	3:29:00.34	31:13:39.50	3:29:00.31	31:13:38.57	0.226	13.160 \pm 0.022	11.946 \pm 0.030	11.337 \pm 0.022	10.981 \pm 0.004	10.998 \pm 0.005	10.905 \pm 0.015	10.921 \pm 0.018	...
162	3:28:55.16	31:14:16.53	3:28:55.06	31:14:16.49	0.094	13.733 \pm 0.039	12.950 \pm 0.054	12.748 \pm 0.099	12.686 \pm 0.131	...
163	3:28:57.24	31:14:19.94	3:28:57.21	31:14:18.91	0.056	8.1920 \pm 0.019	7.7730 \pm 0.017	7.6630 \pm 0.013	7.5757 \pm 0.002	7.5549 \pm 0.003
165	3:29:21.85	31:15:37.42	3:29:21.87	31:15:36.30	0.956	11.176 \pm 0.019	10.151 \pm 0.028	9.5040 \pm 0.018	8.5005 \pm 0.002	8.1994 \pm 0.002	7.9469 \pm 0.004	7.4343 \pm 0.002	4.8150 \pm 0.031
166	3:29:28.17	31:16:29.52	3:29:28.15	31:16:28.57	0.169	13.054 \pm 0.021	12.500 \pm 0.032	12.091 \pm 0.022	11.617 \pm 0.005	11.600 \pm 0.007	11.549 \pm 0.019	11.468 \pm 0.023	...
169	3:29:34.32	31:17:44.45	3:29:34.31	31:17:43.32	0.459	12.026 \pm 0.018	11.312 \pm 0.029	11.065 \pm 0.024	10.784 \pm 0.003	10.816 \pm 0.005	10.770 \pm 0.013	10.719 \pm 0.013	...
171	3:29:46.36	31:20:40.19	3:29:46.40	31:20:39.41	0.973	12.360 \pm 0.019	11.737 \pm 0.028	11.474 \pm 0.025	11.142 \pm 0.004	11.139 \pm 0.006	11.070 \pm 0.015	11.023 \pm 0.018	...
175	3:29:25.99	31:26:41.57	3:29:25.92	31:26:40.15	0.669	>11.005	9.9920 \pm 0.033	>9.5100	8.7161 \pm 0.002	8.2196 \pm 0.002	7.6367 \pm 0.003	6.4602 \pm 0.001	4.2790 \pm 0.031
176	3:29:26.81	31:26:48.33	3:29:26.81	31:26:47.51	0.393	10.832 \pm 0.020	9.9920 \pm 0.027	9.6790 \pm 0.024	9.3966 \pm 0.002	9.4382 \pm 0.003	9.2863 \pm 0.007	8.9351 \pm 0.013	...
179	3:29:04.73	31:11:35.05	3:29:04.73	31:11:34.89	0.798	>18.499	>15.642	14.447 \pm 0.075	11.807 \pm 0.007	10.918 \pm 0.005	10.301 \pm 0.011	9.7087 \pm 0.009	7.2040 \pm 0.033
183	3:29:32.87	31:27:13.51	3:29:32.86	31:27:12.65	0.947	13.353 \pm 0.023	12.598 \pm 0.029	12.285 \pm 0.028	11.509 \pm 0.005	11.369 \pm 0.006	11.175 \pm 0.015	10.625 \pm 0.017	8.5350 \pm 0.036
188	3:29:30.55	31:27:27.10	3:29:30.54	31:27:28.00	1.801	13.808 \pm 0.024	13.014 \pm 0.033	12.598 \pm 0.028	12.195 \pm 0.007	12.142 \pm 0.008	12.107 \pm 0.028	12.096 \pm 0.054	...

^aThe IR detections in multiple bands are matched to <1", with the coordinates at the shortest detected wavelength listed.^bThree sources match to infrared detections with separations >1": 12, 135, 188.

Table 3. NGC 1333: IR Coordinates & *Chandra* ID of X-ray Detected YSOs

<i>Spitzer</i> ID ^a	RA (2000)	Dec (2000)	Class ^b	<i>Chandra</i> ID	G.ID ^c
18	3:28:43.26	31:17:33.11	I	23	9
25	3:28:58.41	31:22:17.64	I	89	38
30	3:29:04.94	31:20:38.59	FS	67	57
31	3:29:07.76	31:21:57.34	I	82	...
34	3:29:09.08	31:23:05.66	I	103	63
36	3:29:12.94	31:18:14.55	I	34	71
45	3:28:43.56	31:17:36.53	FS	26	10
46	3:28:44.08	31:20:52.89	II	137	11
47	3:28:46.18	31:16:38.66	II	13	14
48	3:28:47.63	31:24:06.14	II	110	15
49	3:28:47.82	31:16:55.32	II	17	16
50	3:28:51.02	31:18:18.53	II	36	19
51	3:28:51.06	31:16:32.63	II	128	20
52	3:28:51.19	31:19:54.94	II	53	21
53	3:28:52.13	31:15:47.24	II	2	...
54	3:28:52.15	31:22:45.41	II	99	23
57	3:28:53.93	31:18:09.30	II	32	25
59	3:28:54.61	31:16:51.29	II	16	27
61	3:28:55.07	31:16:28.82	II	11	28
62	3:28:55.14	31:16:24.73	II	10	...
63	3:28:56.08	31:19:08.58	II	43	...
64	3:28:56.31	31:22:28.02	FS	92	...
65	3:28:56.64	31:18:35.67	II	39	30
67	3:28:56.95	31:16:22.26	II	9	32
69	3:28:57.69	31:19:48.12	II	51	35
73	3:28:59.31	31:15:48.48	FS	3	39
74	3:28:59.55	31:21:46.76	II	80	41
75	3:29:00.15	31:21:09.27	II	74	42
76	3:29:02.15	31:16:11.41	II	5	47
77	3:29:02.79	31:22:17.36	II	88	...
78	3:29:03.13	31:22:38.22	II	96	50
79	3:29:03.20	31:25:45.32	II	152	...
80	3:29:03.39	31:18:40.06	II	40	...
82	3:29:03.86	31:21:48.77	II	81	52
85	3:29:04.72	31:11:35.03	II	179	...
88	3:29:05.76	31:16:39.68	II	14	58
91	3:29:07.93	31:22:51.56	II	100	61
97	3:29:10.40	31:21:59.29	II	84	64
103	3:29:11.87	31:21:27.09	FS	78	69
106	3:29:13.12	31:22:52.88	II	101	72
109	3:29:16.59	31:23:49.62	II	109	77
111	3:29:17.66	31:22:45.15	II	98	79
114	3:29:18.72	31:23:25.54	FS	106	81
115	3:29:20.04	31:24:07.57	FS	111	84
116	3:29:20.42	31:18:34.29	II	37	86
118	3:29:21.55	31:21:10.52	II	76	88

Table 3—Continued

<i>Spitzer</i> ID ^a	RA (2000)	Dec (2000)	Class ^b	<i>Chandra</i> ID	G.ID ^c
119	3:29:21.87	31:15:36.39	II	165	90
120	3:29:23.14	31:20:30.46	II	135	...
123	3:29:25.92	31:26:40.12	FS	175	...
125	3:29:29.78	31:21:02.79	II	72	103
126	3:29:30.39	31:19:03.45	II	132	...
128	3:29:32.86	31:27:12.68	II	183	106
136	3:29:26.78	31:26:47.72	TD	176	100
137	3:29:29.26	31:18:34.85	TD	38	102
138	3:28:36.51	31:19:29.07	III	47	4
139	3:28:36.92	31:17:35.49	III	25	6
140	3:28:36.94	31:23:12.13	III	104	5
141	3:28:46.87	31:20:27.66	III	61	...
142	3:28:48.17	31:19:23.49	III	45	...
143	3:28:50.95	31:23:48.00	III	108	...
144	3:28:54.96	31:18:15.35	III	35	...
145	3:28:55.06	31:14:16.49	III	162	...
146	3:28:55.25	31:17:35.42	III	129	...
147	3:28:56.22	31:17:45.75	III	28	...
148	3:28:57.04	31:15:02.85	III	123	...
149	3:29:00.31	31:13:38.60	III	161	43
150	3:29:00.37	31:20:45.71	III	68	44
151	3:29:00.70	31:22:00.82	III	85	45
152	3:29:02.97	31:15:16.73	III	1	49
153	3:29:04.05	31:17:07.58	III	20	53
154	3:29:04.16	31:25:15.16	III	149	54
155	3:29:04.62	31:20:29.03	III	62	...
156	3:29:08.32	31:20:20.45	III	60	...
157	3:29:12.78	31:20:07.60	III	56	70
158	3:29:13.61	31:17:43.55	III	27	...
159	3:29:16.55	31:21:02.49	III	71	...
160	3:29:16.68	31:16:18.24	III	8	78
161	3:29:19.76	31:24:57.17	III	116	...
162	3:29:22.04	31:24:15.41	III	112	91
163	3:29:23.49	31:23:30.94	III	107	93
164	3:29:28.15	31:16:28.64	III	166	101
165	3:29:34.30	31:17:43.42	III	169	107
171	3:29:11.30	31:17:17.67	III	22	67
173	3:29:30.54	31:27:28.02	III	188	...
174	3:29:46.39	31:20:39.52	III	171	...
177	3:29:24.82	31:24:06.23	III	143	...
178	3:28:58.10	31:18:03.79	III	30	36
179	3:29:02.88	31:16:01.16	III	4	48
180	3:28:57.41	31:19:50.63	III	52	34
181	3:28:57.20	31:14:19.08	III	163	33
182	3:28:59.34	31:16:31.51	III	12	...
183	3:29:09.16	31:21:44.56	III	79	...

Table 3—Continued

<i>Spitzer</i> ID ^a	RA (2000)	Dec (2000)	Class ^b	<i>Chandra</i> ID	G.ID ^c
184	3:29:10.79	31:22:30.27	III	94	66
185	3:29:14.43	31:22:36.35	III	95	75
186	3:29:23.69	31:25:09.62	III	148	...

^aIdentifiers from Gutermuth et al. (2008b).

^bEvolutionary classification modified from that of Gutermuth et al. (2008b) based on Winston et al. (2007). I: Class I, FS: Flat Spectrum, II: Class II, TD: Transition Disk, III: Class III.

^cIdentifiers from Getman et al. (2002).

Table 4. Serpens: Spectroscopic & X-ray Properties of YSOs

Sp ID ^a	SpT	Class ^b	Ch ID	$\log(\frac{L_{bol}}{L_{\odot}})$	T_{eff} [K]	$\log(\frac{SA}{SA_{\odot}})$	L_X [$ergs^{-1}$]	kT [keV]	N_H [$\times 10^{22}$]	A_K ^c [mag.]	Age ^d [Myr]	Mass ^d [M_{\odot}]
9	K8.0 \pm 1.5	O/I	67	-0.179	3892	3.22	28.57	1.30	0.86	...	1.5	1.01
27	K7.0 \pm 3.5	FS	74	0.265	3997	8.09	29.40	2.01	0.65	0.94	\sim 0.2	1.20
33	M4.5 \pm 1.0	FS	...	-0.867	3197	1.45	0.11	1.4	0.23
36	K6.5 \pm 2.5	FS	9	0.853	4147	27.1	0.95	\sim 0.2	1.13
40	M0.0 \pm 1.5	FS	44	-0.090	3821	4.26	29.02	1.80	0.86	0.94	0.9	0.95
53	M4.0 \pm 2.0	II	...	-1.281	3299	0.49	0.21	9.0	0.25
54	M9.0 \pm 5.0	II	...	-1.778	2400	0.56	0.27	\sim 0.2	0.02
59	K7.5 \pm 1.5	II	77	0.356	3955	10.4	29.35	4.22	0.38	0.57	\sim 0.2	1.18
65	K7.0 \pm 1.5	II	...	-0.384	4060	1.70	0.68	6.2	1.01
66	M5.0 \pm 5.0	II	...	-1.952	3154	0.12	12.9	0.13
67	M4.5 \pm 1.5	II	...	-1.219	3226	0.62	0.53	5.6	0.22
68	M8.7 \pm 5.0	II	...	-1.673	2493	0.61	0.98	\sim 0.2	0.02
71	M9.0 \pm 2.5	II	...	2.069	2400	3962	1.23
73	M2.5 \pm 1.5	II	86	0.175	3487.5	11.3	29.70	2.41	0.51	0.70	\sim 0.2	0.75
74	M4.0 \pm 1.5	II	...	-0.878	3241	1.34	0.29	1.8	0.25
78	M0.0 \pm 1.5	II	84	0.018	3850	5.32	29.57	2.92	0.42	0.79	0.6	1.01
79	M2.0 \pm 1.5	II	...	-0.685	3560	1.43	0.23	5.1	0.52
81	M2.0 \pm 1.5	II	60	-0.039	3560	6.36	30.03	3.53	0.78	0.58	\sim 0.2	0.70
82	A7.0 \pm 2.5	II	...	1.129	7850	3.96	0.	5.4	...
83	K2.0 \pm 1.5	II	71	0.926	4900	16.4	29.50	3.53	0.90	2.76	\sim 0.2	1.37
84	M1.0 \pm 1.5	II	42	-0.383	3705	2.45	29.51	1.25	0.69	0.37	2.0	0.75
85	M3.0 \pm 1.5	II	68	0.406	3270	24.9	29.91	6.00	1.54	0.27	\sim 0.2	0.55
87	M8.0 \pm 1.5	II	61	-1.382	2710	0.85	0.02	\sim 0.2	0.05
88	M7.5 \pm 1.5	II	...	-1.551	2778	0.53	0.	\sim 0.2	0.05
91	M5.5 \pm 1.5	II	...	-1.691	3098	0.24	0.11	8.0	0.11
94	M1.5 \pm 1.0	II	57	-0.430	3647	2.34	29.02	2.87	0.36	0.95	2.1	0.67
96	M4.5 \pm 2.5	II	...	-0.701	3226.5	2.05	0.76	1.1	0.26
98	M5.0 \pm 1.5	II	85	-0.908	3125	1.44	0.24	1.1	0.19
100	M4.5 \pm 1.5	II	59	-0.608	3415.5	2.03	29.20	1.62	0.09	0.36	1.9	0.40
101	M4.0 \pm 1.0	II	87	-0.861	3255	1.37	30.65	4.07	0.49	0.13	1.8	0.26
102	M5.0 \pm 5.0	II	...	-2.102	3111	0.09	0.	13.8	0.11
103	K2.5 \pm 1.5	II	...	0.421	4832	5.42	0.42	2.4	1.37
104	M0.5 \pm 1.5	II	...	0.137	3763	7.65	0.83	\sim 0.2	0.97
105	K1.0 \pm 1.5	II	73	1.646	5080	74.5	31.12	3.23	3.10	3.69	\sim 0.2	...
122	M3.5 \pm 1.5	TD	...	1.694	3342.5	443.	0.89
124	K6.5 \pm 4.5	TD	...	0.090	4161	4.59	0.	1.0	1.31
127	M2.0 \pm 1.5	TD	...	1.091	3560	85.9	1.33
128	M3.5 \pm 1.5	TD	46	-0.934	3371	1.01	29.05	0.98	0.38	0.06	4.9	0.33
134	M2.0 \pm 1.5	TD	...	1.203	3560	111.	1.35
156	M2.0 \pm 5.0	TD	...	-0.421	3589	2.56	0.90	1.8	0.60
157	M1.0 \pm 3.5	TD	45	-0.989	3690	0.618	29.27	0.87	0.53	0.24	14.6	0.61
158	M1.0 \pm 1.5	TD	...	2.949	3705	5290.	6.26
166	M5.0 \pm 1.0	TD	...	-0.779	3125	1.94	0.46	0.8	0.22
170	M3.5 \pm 1.5	TD	...	1.131	3342.5	121.	1.06
176	M4.0 \pm 1.5	TD	...	0.433	3270	26.5	1.32	\sim 0.2	0.56

Table 4—Continued

<i>Sp</i> ID ^a	SpT	Class ^b	<i>Ch</i> ID	$\log(\frac{L_{bol}}{L_{\odot}})$	T_{eff} [K]	$\log(\frac{SA}{SA_{\odot}})$	L_X [<i>ergs</i> ⁻¹]	kT [keV]	N_H [$\times 10^{22}$]	A_K ^c [mag.]	Age ^d [Myr]	Mass ^d [M_{\odot}]
190	M2.0 \pm 1.5	III	88	0.101	3560	8.80	29.14	1.84	0.37	1.08	\sim 0.2	0.78
192	A0.0	III	69	1.884	9520	10.4	29.47	0.80	0.01	0.	\sim 0.2	...
193	A0.0	III	50	1.480	9520	4.11	2.76	1.6	...
196	M5.0 \pm 1.5	III	76	-0.309	3125	5.75	29.01	10.2	0.010	1.10	\sim 0.2	0.29
199	M2.5 \pm 1.5	III	40	0.308	3487.5	15.4	29.63	2.48	0.45	2.71	\sim 0.2	0.76
201	M5.0 \pm 1.0	III	62	-1.309	3125	0.57	28.62	1.01	0.01	0.	3.7	0.15
203	M5.0 \pm 1.5	III	51	-1.715	3125	0.22	0.02	9.2	0.12
204	M8.5 \pm 5.0	III	65	-1.581	2524	0.72	0.29	\sim 0.2	0.02
205	K5.0 \pm 1.5	III	64	-0.374	4350	1.32	29.75	2.34	0.17	0.16	11.0	1.01
209	M4.5 \pm 1.5	III	41	-0.672	3197.5	2.27	29.11	1.91	0.45	0.79	0.9	0.26
215	M7.0 \pm 1.5	III	58	-0.345	2880	7.34	29.36	4.25	0.80	0.11	\sim 0.2	0.22
216	M0.5 \pm 1.5	III	80	0.698	3777.5	27.4	30.03	2.94	1.09	1.68	\sim 0.2	0.96
220	A3.0	III	36	0.223	8720	0.32	0.	17.5	1.33
221	K7.5 \pm 1.5	III	37	-0.007	3955	4.50	29.70	1.35	0.34	0.47	0.9	1.09
225	G2.5 \pm 1.0	III	56	0.688	5851	4.66	30.31	2.25	0.37	0.47	8.1	...
230	K5.0 \pm 2.5	[III]	...	-0.037	4321	2.94	0.69	2.7	1.26
232	M1.0 \pm 5.0	[III]	...	-0.240	3705	3.41	0.59	1.2	0.78
233	M4.5 \pm 2.0	[III]	...	-1.285	3197	0.55	0.47	5.6	0.19
235	K6.5 \pm 4.0	[III]	...	-0.417	4161	1.42	0.62	8.8	0.98

^a*Sp*: *Spitzer*, *Ch Chandra*. See Tables 6 & 4 of Winston et al. (2009) for coordinates and magnitudes associated with spectra.

^b0/I: Class 0/I, FS: flat spectrum, II: Class II, TD: Transition Disk, III: X-ray Detected Class III. The [III] are the new candidate Class IIIs with detected *Li I* absorption.

^cA value of zero indicates that the source was blueward of the CTTS locus, a null value indicates a value could not be calculated.

^dIsochronal Age and Mass are determined by interpolation from the Baraffe (1998) tracks. Age of \sim 0.2 indicates the source is very young but on edge of isochrone grid.

Table 5. NGC 1333: Spectroscopic & X-ray Properties of YSOs

<i>Sp</i> ID ^a	SpT	Class ^b	<i>Ch</i> ID ^b	$\log(\frac{L_{bol}}{L_{\odot}})$	T_{eff} [K]	$\log(\frac{SA}{SA_{\odot}})$	L_X [<i>ergs</i> ⁻¹]	kT [keV]	N_H [$\times 10^{22}$]	A_K ^c [mag.]	Age ^d [Myr]	Mass ^d [M_{\odot}]
18	K7.0 \pm 1.0	0/I	23	0.066	4089	4.670	29.93	3.95	2.78	...	0.9	1.23
45	M5.0 \pm 1.0	II	26	-0.420	3125	4.461	29.71	3.73	0.35	0.41	\sim 0.2	0.23
46	M7.5 \pm 1.0	II	137	-1.533	2829	0.511	27.88	1.29	...	0.22	0.6	0.06
47	M3.0 \pm 1.5	II	13	-0.101	3415	6.514	29.65	1.04	0.11	0.26	\sim 0.2	0.58
48	M4.0 \pm 1.5	II	110	-0.793	3270	1.576	28.88	2.22	0.89	0.83	1.6	0.28
49	M8.0 \pm 1.0	II	17	-0.918	2710	2.504	28.85	2.32	0.18	0.27	\sim 0.2	0.05
50	M4.5 \pm 1.0	II	36	-0.051	3197.5	9.516	29.12	6.11	0.17	0.41	\sim 0.2	0.44
51	M4.0 \pm 1.0	II	128	-1.250	3255.5	0.560	27.85	3.25	...	0.04	7.0	0.23
52	K7.0 \pm 1.0	II	53	0.005	4039	4.262	30.05	1.72	0.32	0.57	1.1	1.17
53	M7.0 \pm 2.0	II	2	-1.361	2846	0.742	28.11	0.96	0.10	0.	\sim 0.2	0.07
54	M2.5 \pm 1.5	II	99	-0.467	3473	2.623	29.54	2.44	0.13	0.29	1.8	0.48
55	M5.0 \pm 1.0	II	...	-1.440	3154	0.410	0.	6.2	0.16
57	K7.0 \pm 1.5	II	32	0.156	4060	5.903	29.90	2.19	1.29	1.94	0.5	1.22
58	M5.0 \pm 1.0	II	...	-0.910	3098	1.492	0.29	0.9	0.18
59	M1.0 \pm 2.5	II	16	-0.096	3734	4.614	29.72	2.90	0.52	0.93	0.8	0.85
61	M3.0 \pm 1.5	II	11	-0.200	3415	5.193	28.36	2.37	0.81	1.20	0.6	0.54
62	M0.5 \pm 1.5	II	10	-0.453	3792	1.905	29.03	5.17	0.28	0.65	3.9	0.83
64	M2.0 \pm 1.5	II	92	-0.129	3560	5.171	28.51	1.83	0.96	2.18	0.5	0.66
65	M1.5 \pm 1.5	II	39	0.011	3632.5	6.598	29.56	2.41	0.75	0.80	\sim 0.2	0.78
67	M2.5 \pm 1.5	II	9	-0.204	3487.5	4.733	28.20	2.37	0.41	1.30	0.7	0.58
69	M3.5 \pm 1.5	II	51	-0.854	3371.5	1.211	29.79	2.85	0.24	0.32	3.6	0.33
71	M6.0 \pm 1.5	II	...	-1.473	2990	0.471	0.42	2.4	0.09
73	K2.0 \pm 1.5	II	3	1.195	4900	30.44	30.48	2.39	1.46	3.53	\sim 0.2	1.37
76	M3.5 \pm 1.0	II	5	-1.811	3371.5	0.133	28.48	0.84	0.02	0.	17.6	0.26
78	M2.5 \pm 1.0	II	96	-0.970	3458.5	0.838	28.49	...	0.74	0.36	8.4	0.41
82	K6.0 \pm 1.5	II	81	0.161	4234	5.057	30.08	2.40	0.54	0.54	0.9	1.38
88	A3	II	14	1.394	8720	4.799	29.89	3.40	1.36	2.18	2.5	...
91	M2.5 \pm 1.5	II	100	-0.283	3487.5	3.948	29.81	2.21	1.34	1.16	1.1	0.34
94	M5.0 \pm 1.0	II	...	-1.410	3098	0.473	0.26	4.1	0.14
101	M4.0 \pm 1.5	II	...	-0.913	3270	1.196	1.27	2.4	0.26
104	M4.5 \pm 1.5	II	...	-1.265	3154	0.613	0.07	4.0	0.17
105	M8.0 \pm 1.0	II	...	-2.212	2710	0.127	0.	6.3	0.04
106	M3.0 \pm 1.5	II	101	-0.076	3415	6.899	28.92	2.41	1.10	1.02	\sim 0.2	0.59
109	M3.0 \pm 1.0	II	109	-0.492	3444	2.562	29.48	2.69	0.66	0.81	1.7	0.45
111	M0.0 \pm 1.5	II	98	0.432	3821	14.21	30.72	2.46	0.28	0.31	\sim 0.2	1.00
114	M0.0 \pm 1.5	II	106	-0.404	3892	1.923	29.65	1.03	0.20	0.08	4.4	0.93
116	K6.0 \pm 1.5	II	37	0.035	4205	3.885	29.47	4.05	2.07	1.55	1.4	1.31
118	M4.5 \pm 1.5	II	76	-0.967	3197.5	1.155	29.13	1.28	0.17	...	1.9	0.22
119	K4.0 \pm 3.0	II	165	-0.026	4566	2.423	29.51	3.21	3.38	0.21	5.5	1.28
120	M4.5 \pm 1.5	II	135	-0.939	3197.5	1.230	28.26	0.84	0.34	...	1.8	0.22
121	M4.5 \pm 1.5	II	...	-1.257	3197.5	0.591	0.16	5.2	0.19
125	M4.5 \pm 1.5	II	72	-0.687	3197.5	2.201	28.73	2.10	0.09	0.38	0.9	0.26
127	M3.0 \pm 1.0	II	...	-0.994	3429.5	0.819	0.38	8.0	0.38
128	M4.5 \pm 1.5	II	183	-1.260	3226.5	0.567	28.69	3.32	...	0.08	6.2	0.21
131	M7.0 \pm 1.5	II	...	-1.723	2891	0.302	0.	3.8	0.06

Table 5—Continued

<i>Sp</i> ID ^a	SpT	Class ^b	<i>Ch</i> ID ^b	$\log(\frac{L_{bol}}{L_{\odot}})$	T_{eff} [K]	$\log(\frac{SA}{SA_{\odot}})$	L_X [<i>ergs</i> ⁻¹]	kT [keV]	N_H [$\times 10^{22}$]	A_K ^c [mag.]	Age ^d [Myr]	Mass ^d [M_{\odot}]
133	M4.5 \pm 1.5	II	...	-0.733	3197.5	1.978	0.	1.1	0.25
136	K7.5 \pm 1.5	TD	176	-0.019	3997	4.197	30.45	1.34	0.15	0.22	1.1	1.13
137	K7.5 \pm 1.5	III	38	-0.308	3997	2.158	30.28	5.18	0.44	0.64	3.5	1.02
138	M4.0 \pm 1.5	III	47	-1.076	3299	0.793	28.73	0.86	0.11	0.07	5.5	0.27
139	M0.0 \pm 1.5	III	25	0.009	3850	5.213	29.81	2.04	0.29	0.74	0.7	1.01
140	M1.0 \pm 1.0	III	104	-0.294	3690.5	3.064	29.81	1.35	0.20	0.38	1.4	0.75
143	M4.0 \pm 1.5	III	108	-0.139	3270	7.100	29.80	2.58	1.59	1.74	\sim 0.2	0.48
149	M3.0 \pm 1.5	III	161	-0.707	3415	1.614	29.96	2.28	0.32	0.54	2.6	0.38
150	M4.5 \pm 1.5	III	68	-0.890	3226.5	1.331	28.39	1.14	0.34	0.54	1.7	0.24
151	M1.5 \pm 1.5	III	85	-0.017	3632.5	6.172	29.09	1.44	1.24	2.43	\sim 0.2	0.77
154	M2.0 \pm 1.5	III	149	-0.169	3560	4.719	29.05	2.54	0.76	1.25	0.7	0.65
156	M4.0 \pm 1.5	III	60	-0.703	3270	1.938	29.00	0.71	1.88	1.17	1.3	0.29
157	M7.5 \pm 1.5	III	56	-1.796	2812	0.285	29.16	0.34	0.87	0.15	3.3	0.05
159	M2.0 \pm 1.5	III	71	-0.911	3560	0.854	28.34	1.72	0.96	1.02	10.3	0.51
160	M3.5 \pm 1.5	III	8	-0.565	3342.5	2.441	29.26	1.08	...	0.	1.3	0.36
161	A0	III	116	1.404	9520	3.462	29.31	0.95	0.74	0.	2.4	...
162	M3.5 \pm 1.0	III	112	-0.713	3386	1.648	29.01	1.05	...	0.09	2.1	0.36
163	M3.5 \pm 1.5	III	107	-0.654	3342.5	1.987	29.94	2.24	0.29	0.51	1.5	0.34
164	M7.5 \pm 1.0	III	166	-1.377	2761	0.807	29.22	1.12	0.06	0.	\sim 0.2	0.06
165	M3.0 \pm 1.5	III	169	-0.730	3444	1.481	29.99	2.46	0.04	0.08	3.3	0.41
167	M3.0 \pm 1.5	[III]	...	-0.626	3444	1.880	0.34	2.4	0.42
170	M3.5 \pm 1.0	[III]	...	-2.116	3313.5	0.071	0.	19.3	0.17
174	M4.5 \pm 1.5	III	171	-0.968	3226.5	1.110	29.04	0.86	0.18	0.	2.3	0.24
175	M3.0 \pm 1.0	[III]	...	-1.783	3386	0.140	0.	17.8	0.27
176	M3.0 \pm 1.5	[III]	...	-0.696	3429.5	1.627	0.26	2.7	0.39
177	M6.5 \pm 1.5	III	143	-1.856	2957	0.204	28.10	0.94	...	0.	6.9	0.07
178	M0.5 \pm 1.0	III	30	-0.552	3748.5	1.588	29.31	1.00	0.53	0.53	5.3	0.76
179	M1.5 \pm 1.0	III	4	-1.077	3618	0.546	29.08	1.00	...	0.01	14.9	0.56
180	M4.0 \pm 1.5	III	52	-0.379	3284.5	4.020	29.55	0.77	0.70	0.50	0.6	0.36

^a*Sp*: *Spitzer*, *Ch Chandra*. See Table 2 & Tables 2 & 3 of Gutermuth et al. (2008b) for coordinates and magnitudes associated with spectra.

^b0/I: Class 0/I, FS: flat spectrum, II: Class II, TD: Transition Disk, III: X-ray Detected Class III. The [III] are the new candidate Class IIIs with detected *Li I* absorption.

^cA value of zero indicates that the source was blueward of the CTTS locus, a null value indicates a value could not be calculated.

^dIsochronal Age and Mass are determined by interpolation from the Baraffe (1998) tracks. Age of \sim 0.2 indicates the source is very young but on edge of isochrone grid.

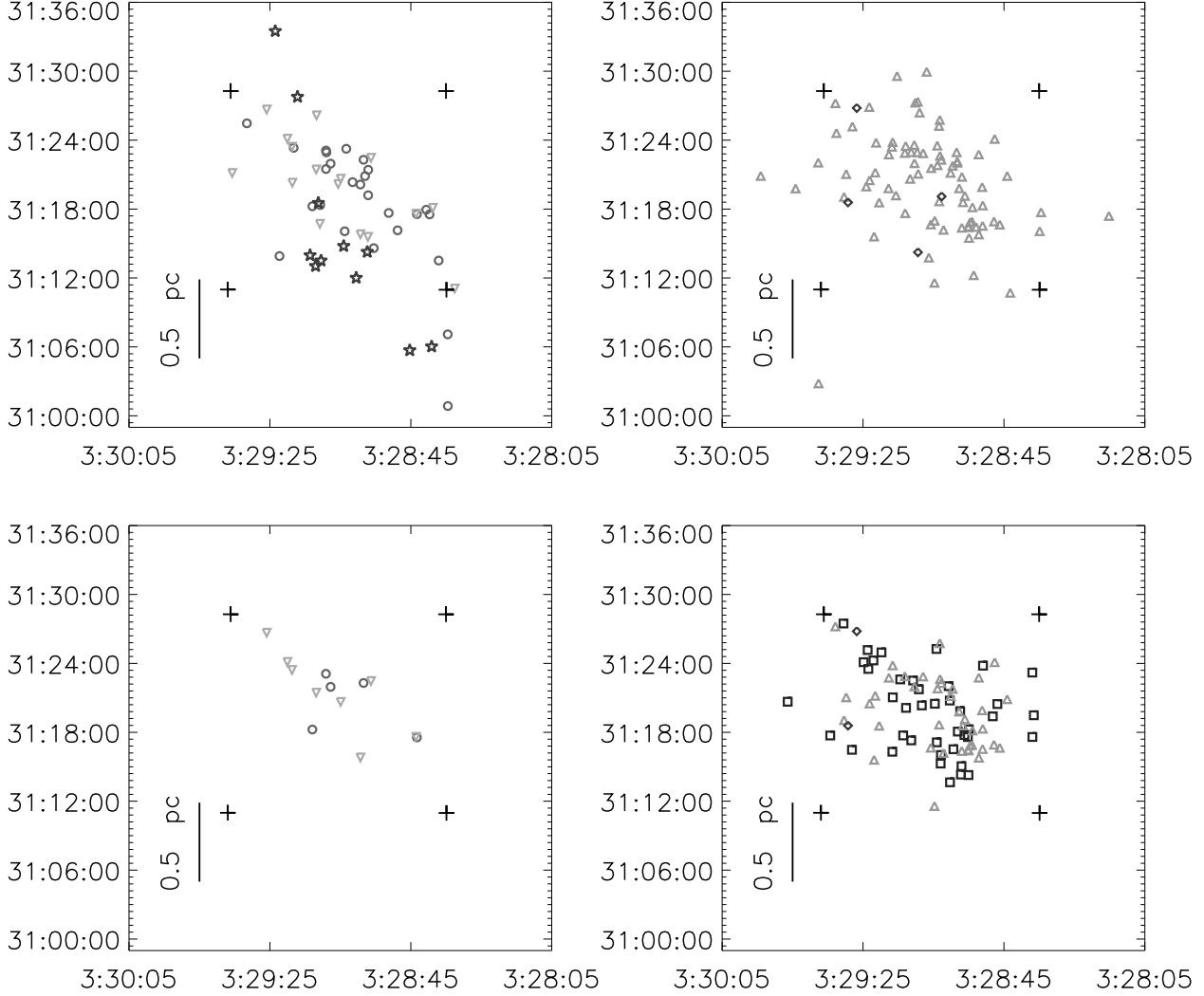


Fig. 1.— *Above:* Graphs of the spatial distribution of the various classes of YSOs in NGC 1333. *Upper Left:* Class 0, Class I and Flat Spectrum sources, in stars, circles and inverted triangles, respectively. *Upper Right:* Class II (triangles) and Transition Disk members (diamonds). *Lower Left:* X-ray selected sample of Class 0/I and Flat Spectrum objects. *Lower Right:* X-ray selected sample of the Class II, Transition Disk, and Class III members (shown by squares). The elongated distribution of the protostellar objects can be observed, while the Class II and later classes follow a more dispersed pattern over the region. The four crosses outline the *Chandra* FOV.

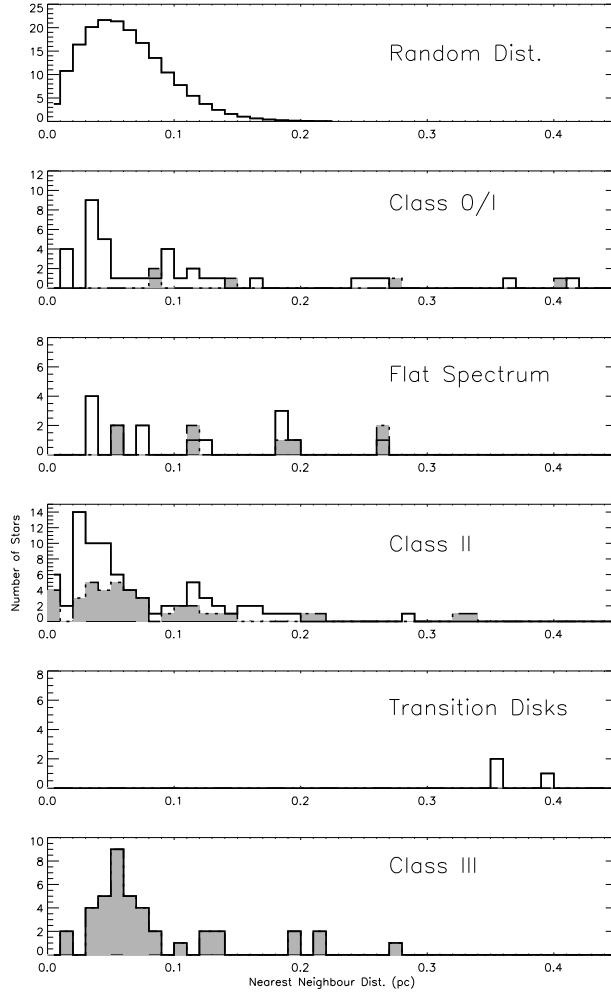


Fig. 2.— Histograms of the nearest neighbour distances of the NGC 1333 YSOs by advancing evolutionary class: Class 0/I, Flat Spectrum, Class II, Transition Disk, Class III. The topmost graph plots the random distribution. The solid grey histograms indicates the distribution of the nearest neighbor distances calculated using only the X-ray detected sources in each class.

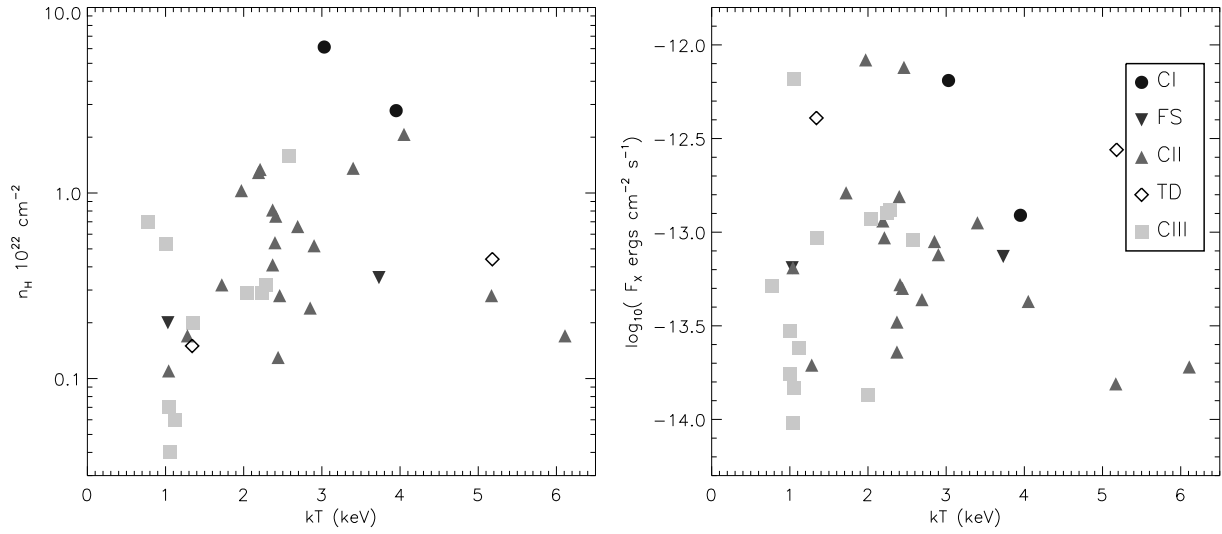


Fig. 3.— *Left:* Plasma temperature (kT) against Hydrogen column density (N_H). The Class 0/I and Flat Spectrum sources show higher N_H , consistent with the presence of an infalling envelope. The Class II sources have higher median N_H values than the Class III sources. *Right:* The plasma temperature plotted against the log of the X-ray flux (F_X). A weak trend of increasing flux with kT is present. There is a significant difference in the value of kT between the Class IIs and Class IIIs. The symbols are as follows: Class 0/I, circle; Flat Spectrum, inverted triangle; Class II, triangle; Transition Disk, diamond; Class III, squares.

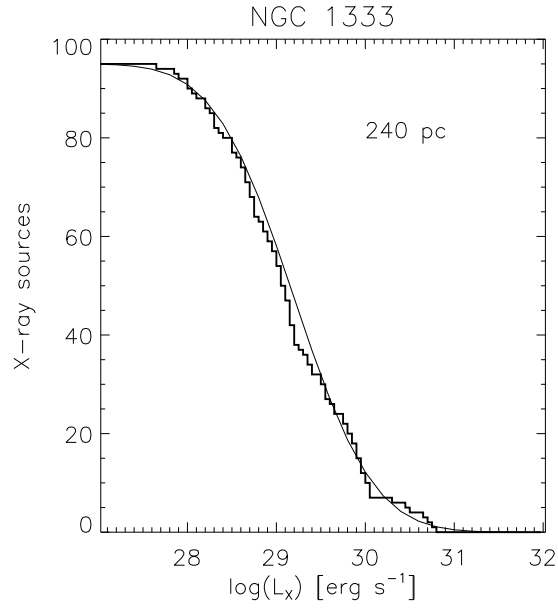


Fig. 4.— X-ray Luminosity Function of all *Chandra* detected sources for which flux measurements were determined in NGC 1333. The data are fit to a log-normal distribution with $\langle \log(L_X[\text{ergs}^{-1}]) \rangle = 29.3$ and $\sigma = 1.0$, as determined by Feigelson et al. (2005) for Orion, IC 348 and NGC 1333.

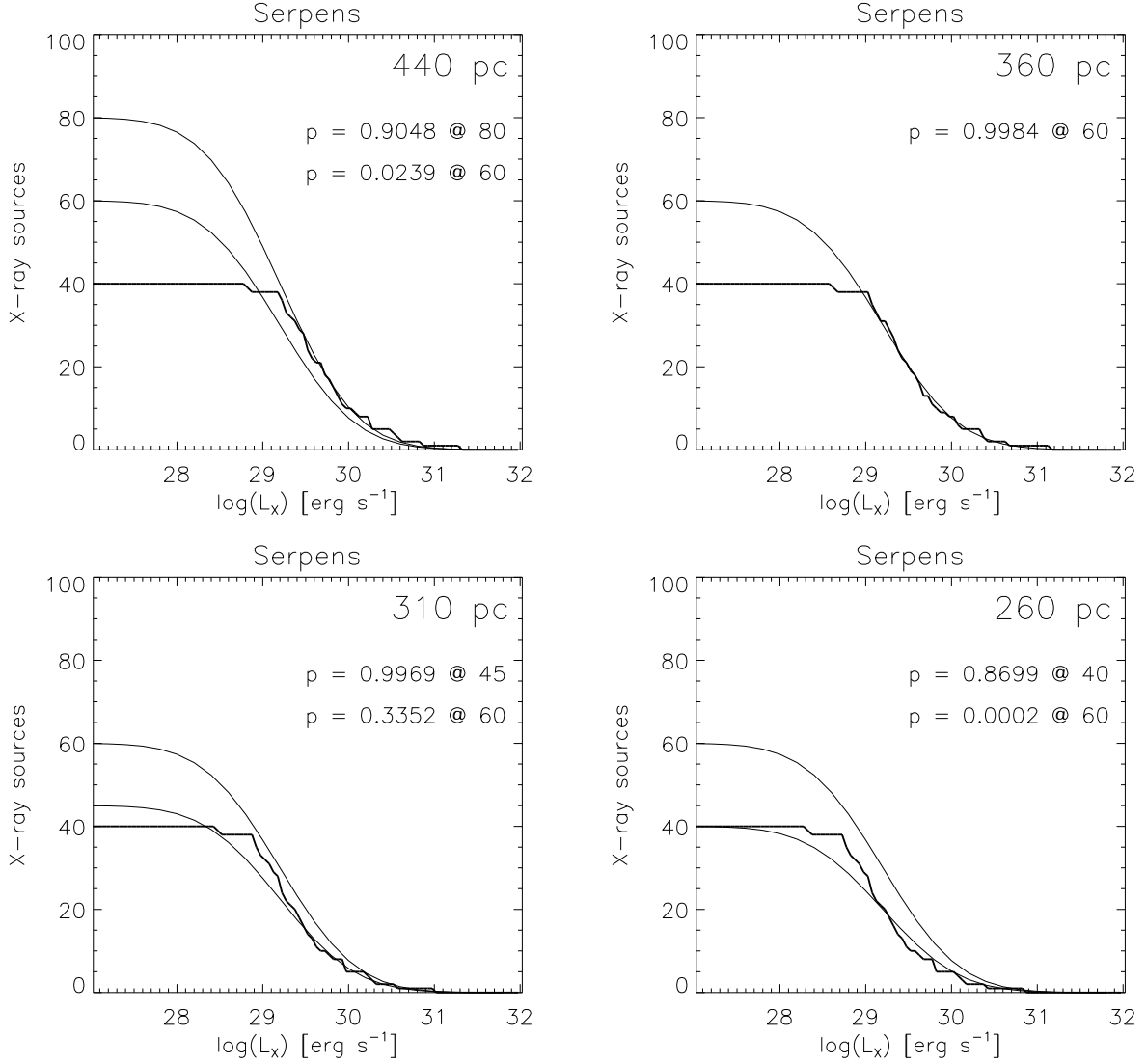


Fig. 5.— X-ray Luminosity Functions for the Serpens *Chandra* detected sources for which flux measurements were determined. The XLFs are given for four different distances to the Serpens Core: 440pc, 310pc, 260pc (previous distance estimates from the literature, see text), and 360pc, the best fit to the log-normal distribution from these data. The data were fit to a log-normal distribution with $\langle \log(L_X[\text{ergs}^{-1}]) \rangle = 29.3$ and $\sigma = 1.0$, as determined by Feigelson et al. (2005) for Orion, IC 348 and NGC 1333. The fit is performed on the tail of the distributions above $\log(L_X[\text{ergs}^{-1}]) = 29.3$ where the luminosity bins are considered to be complete and the universal XLF is best defined. The minimum χ^2 fit is overplotted for the case where the number of X-ray detected objects is a free parameter and for the case where the number of objects is constrained to 60 sources. The probabilities associated with both of these fits is also given.

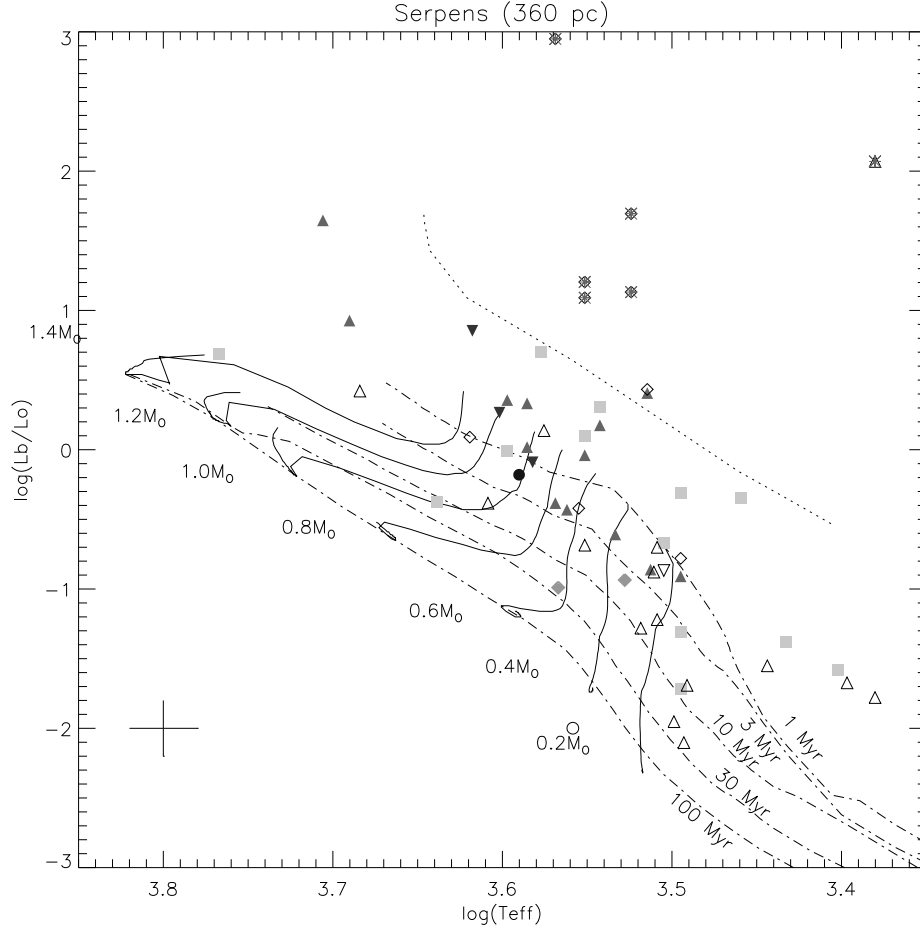


Fig. 6.— The H-R diagram of the Serpens cluster plotting all stars with well established spectral types, using a distance of 360 pc to calculate the luminosity. The sources are identified by their evolutionary classification, with circles indicating the Class 0/I protostars, the inverted triangles the Flat Spectrum. The Class II objects are represented by triangles, Transition Disks by open diamonds, and Class III sources by squares. The filled symbols plot those sources with *Chandra* X-ray counterparts, the empty symbols, those without. The evolutionary tracks are taken from Baraffe (1998), with the 1, 3, 10, 30, and 100 Myr isochrones, and mass tracks from 0.2 to $1.4 M_{\odot}$. The stellar birthline is plotted as a dotted line (D’Antona & Mazzitelli 1997). The six highly luminous objects, four Transition Disks and one Class II object without X-rays, are very likely contaminating AGB stars, and are marked with asterisks (see Winston et al. 2009, for a discussion of these objects). The error bars for typical uncertainties are shown in the lower left corner.

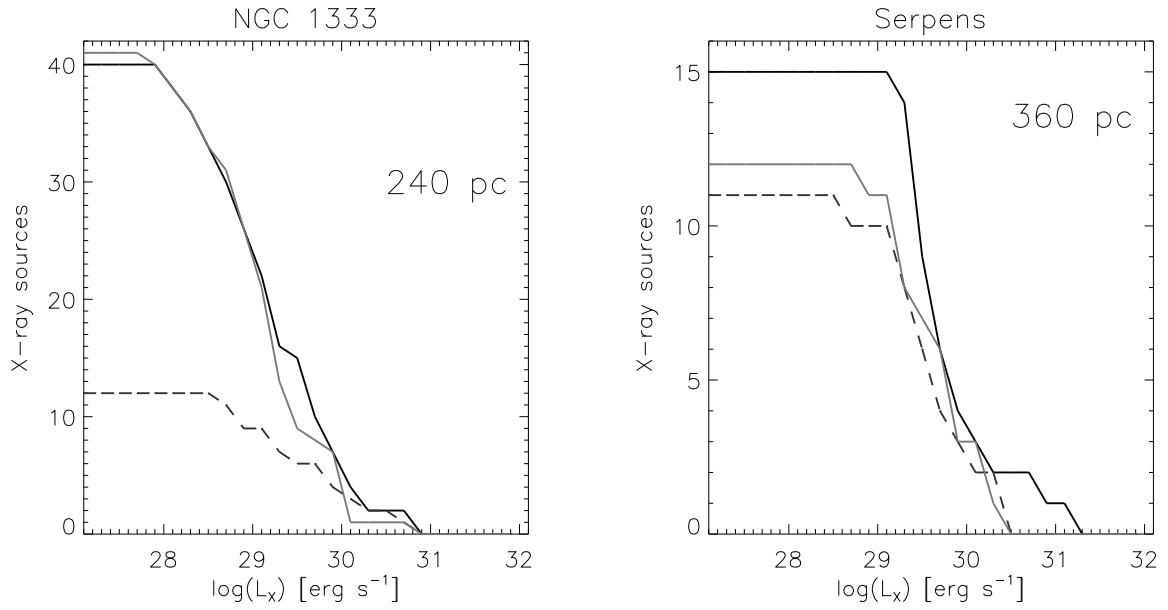


Fig. 7.— X-ray Luminosity Functions of NGC 1333 and Serpens for sources with absorption corrected luminosities. The Class II sources are shown by the solid black line, the Class III by the grey line. The dashed black line indicates the protostars (Class 0/I and Flat Spectrum). In both clusters, the K-S probabilities suggest that the three groups are from the same parent distribution.

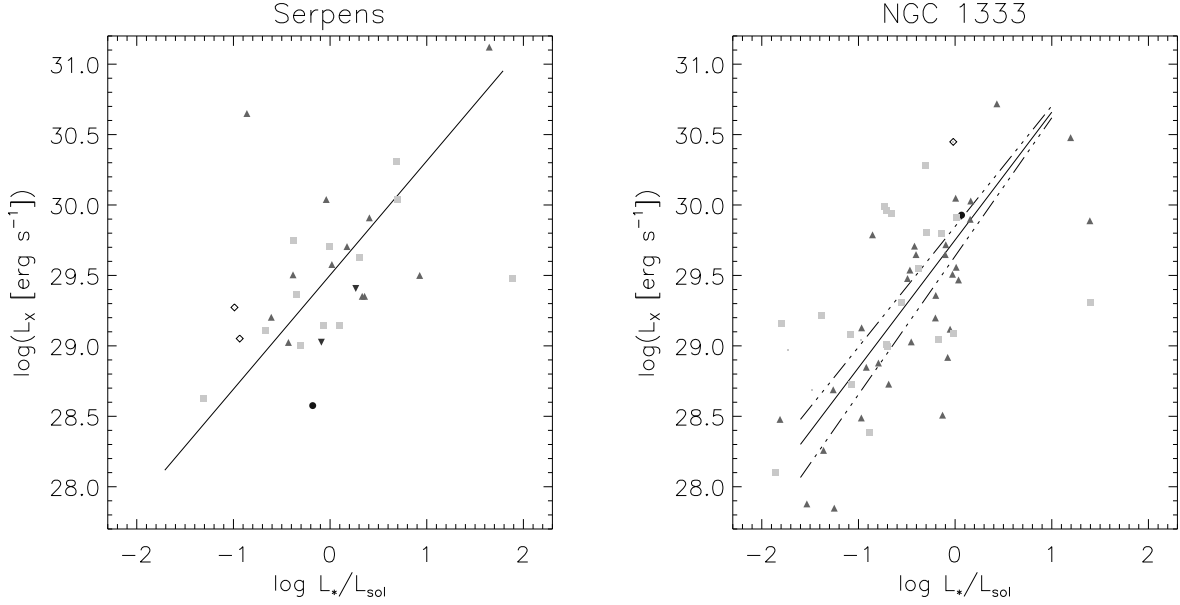


Fig. 8.— In the graphs, the X-ray luminosity, L_X , is plotted against the bolometric luminosity, L_*/L_\odot , for the Serpens (left) and NGC 1333 (right) clusters. A linearly increasing trend is observed in both, with slopes consistent with previous observations of the Orion Nebular Cluster and IC 348. Symbols indicate Class 0/I (circle), Flat Spectrum (inverted triangle), Class II (triangle), Transition Disk (diamond), Class III (square). The dot-dashed lines indicate the best fit to the entire YSO sample in each region, with $\log(L_X[\text{ergs}^{-1}]) \propto (0.82 \pm 0.11) \log(L_*/L_\odot)$ in Serpens and $\log(L_X[\text{ergs}^{-1}]) \propto (0.91 \pm 0.10) \log(L_*/L_\odot)$ in NGC 1333. The dashed lines on the NGC 1333 plot are the fits to the Class III sources (upper line: $\log(L_X[\text{ergs}^{-1}]) = 29.85 \pm 0.19 + (0.86 \pm 0.14) \log(L_*/L_\odot)$) and Class II sources (lower line: $\log(L_X[\text{ergs}^{-1}]) = 29.69 \pm 0.10 + (0.98 \pm 0.13) \log(L_*/L_\odot)$).

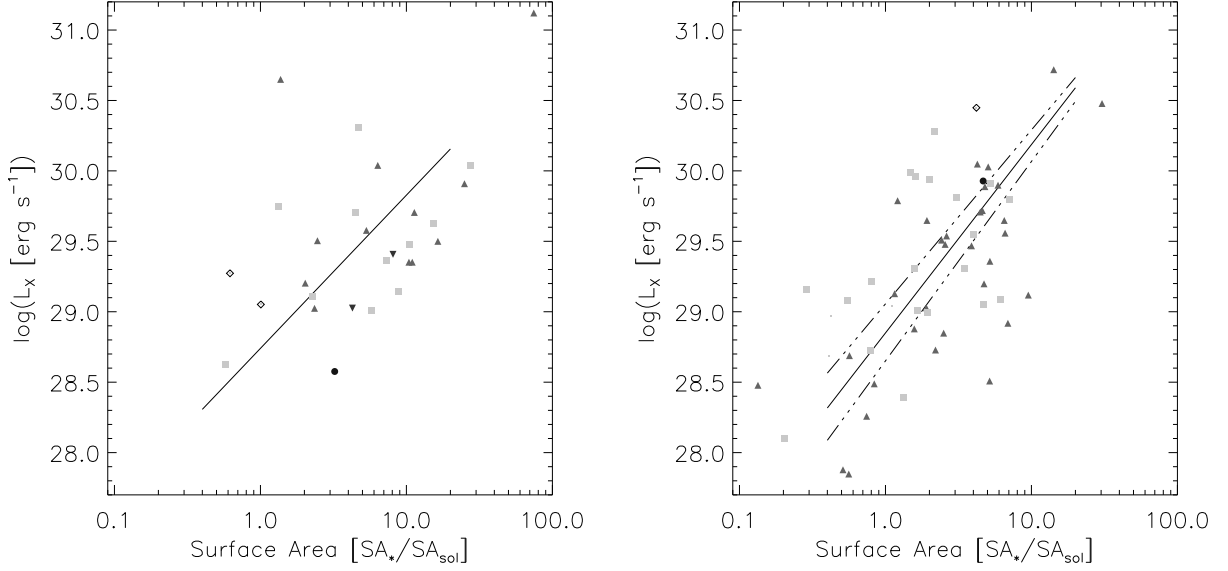


Fig. 9.— In the two plots, the relation of X-ray luminosity, L_X , to the stellar surface area is plotted for Serpens (left) and NGC 1333 (right). There is a trend of increasing surface area with luminosity, where $L_{bol} \propto 4\pi R^2$. Symbols indicate Class 0/I (circle), Flat Spectrum (inverted triangle), Class II (triangle), Transition Disk (diamond), Class III (square). The dot-dashed lines indicate the best fit to the entire YSO sample in each region, with $\log(L_X[\text{ergs}^{-1}]) = 28.74 \pm 0.13 + (1.09 \pm 0.10) \log(SA_*/SA_{sol})$ in Serpens and $\log(L_X[\text{ergs}^{-1}]) = 28.85 \pm 0.08 + (1.34 \pm 0.12) \log(SA_*/SA_{sol})$ in NGC 1333. The dashed lines on the NGC 1333 plot are the fits to the Class III (upper line) and Class II (lower line) subsamples, showing the Class IIIs marginally brighter in L_X than the Class II for a given $S.A.$, with $\log(L_X[\text{ergs}^{-1}]) = 29.06 \pm 0.10 + (1.24 \pm 0.16) \log(SA_*/SA_{sol})$, for the Class III and $\log(L_X[\text{ergs}^{-1}]) = 28.65 \pm 0.13 + (1.42 \pm 0.18) \log(SA_*/SA_{sol})$, for the Class II.

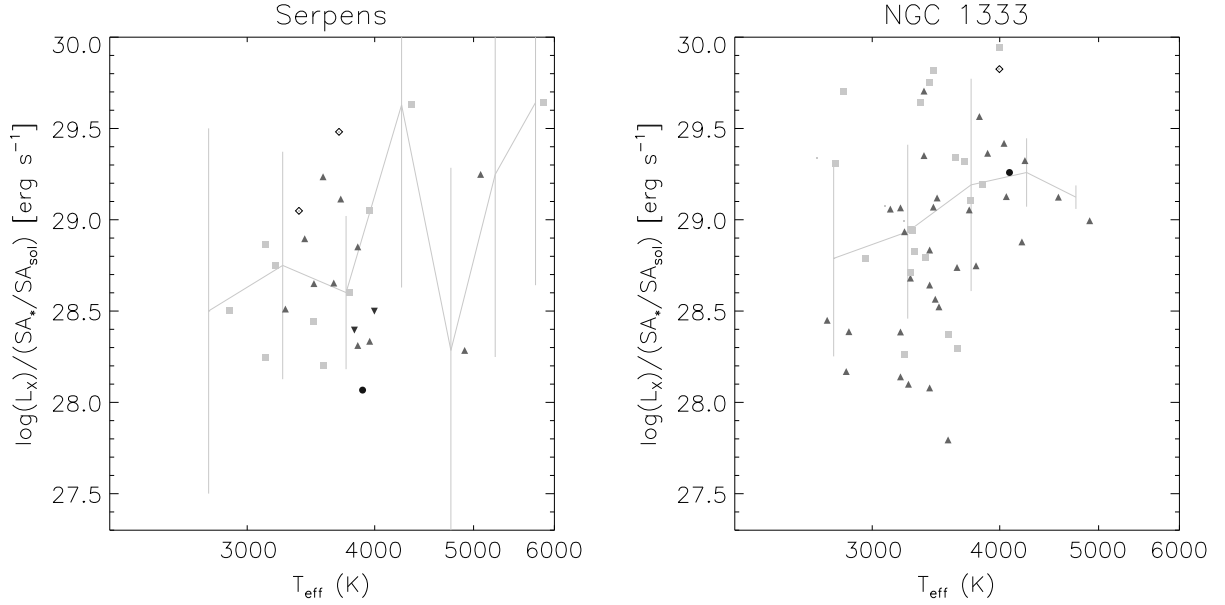


Fig. 10.— In the two graphs, the X-ray luminosity, $L_X/(SA_*/SA_{sol})$, is plotted against the stellar effective temperature, T_{eff} , for the Serpens (left) and NGC 1333 (right) clusters. To remove the effect of surface area, this has been divided out of L_X . A weak increase of $L_X/(SA_*/SA_{sol})$ with T_{eff} is apparent in NGC 1333, with a jump in $L_X/(SA_*/SA_{sol})$ between M0 and K7 spectral types at 3800 K. Symbols indicate Class 0/I (circle), Flat Spectrum (inverted triangle), Class II (triangle), Transition Disk (diamond), Class III (square). The overplotted dashed lines show the median $L_X/(SA_*/SA_{sol})$ in bins of 500 K in T_{eff} from 2500-6000 K. The vertical lines give the standard deviation.

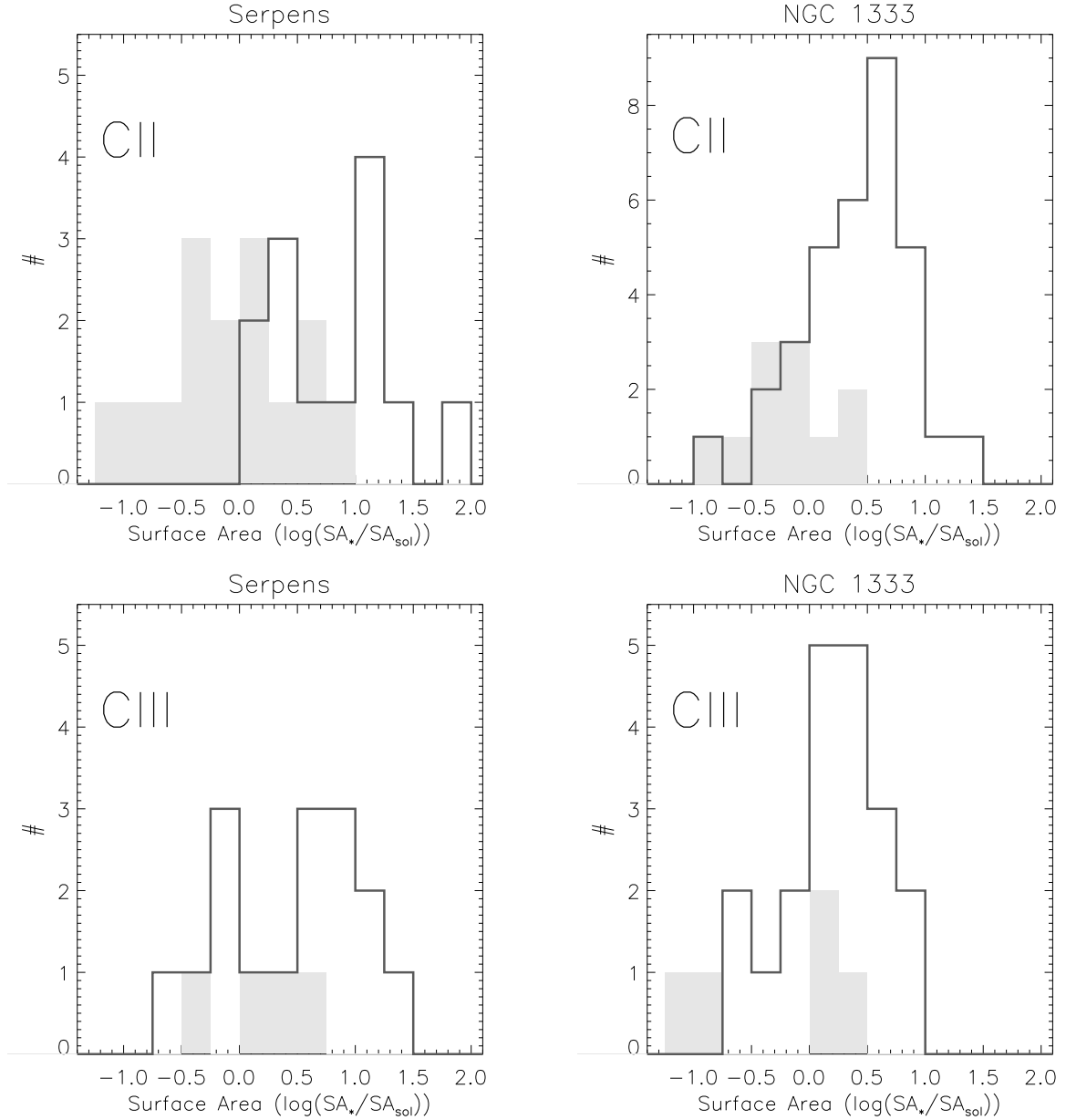


Fig. 11.— Histograms of the stellar surface area, SA_*/SA_{sol} , for the Serpens (left) and NGC 1333 (right) clusters. The upper plots show the Class II sources, the lower plots the Class III. The solid black lines indicate the X-ray detected YSOs. The grey shaded histograms are those of the non X-ray detected YSOs. For the Class IIIs, the non X-ray detections are those identified by *Li I* absorption in their spectra, c.f. Winston et al. (2009). Those sources detected in X-rays have, on average, larger surface areas than those not detected.

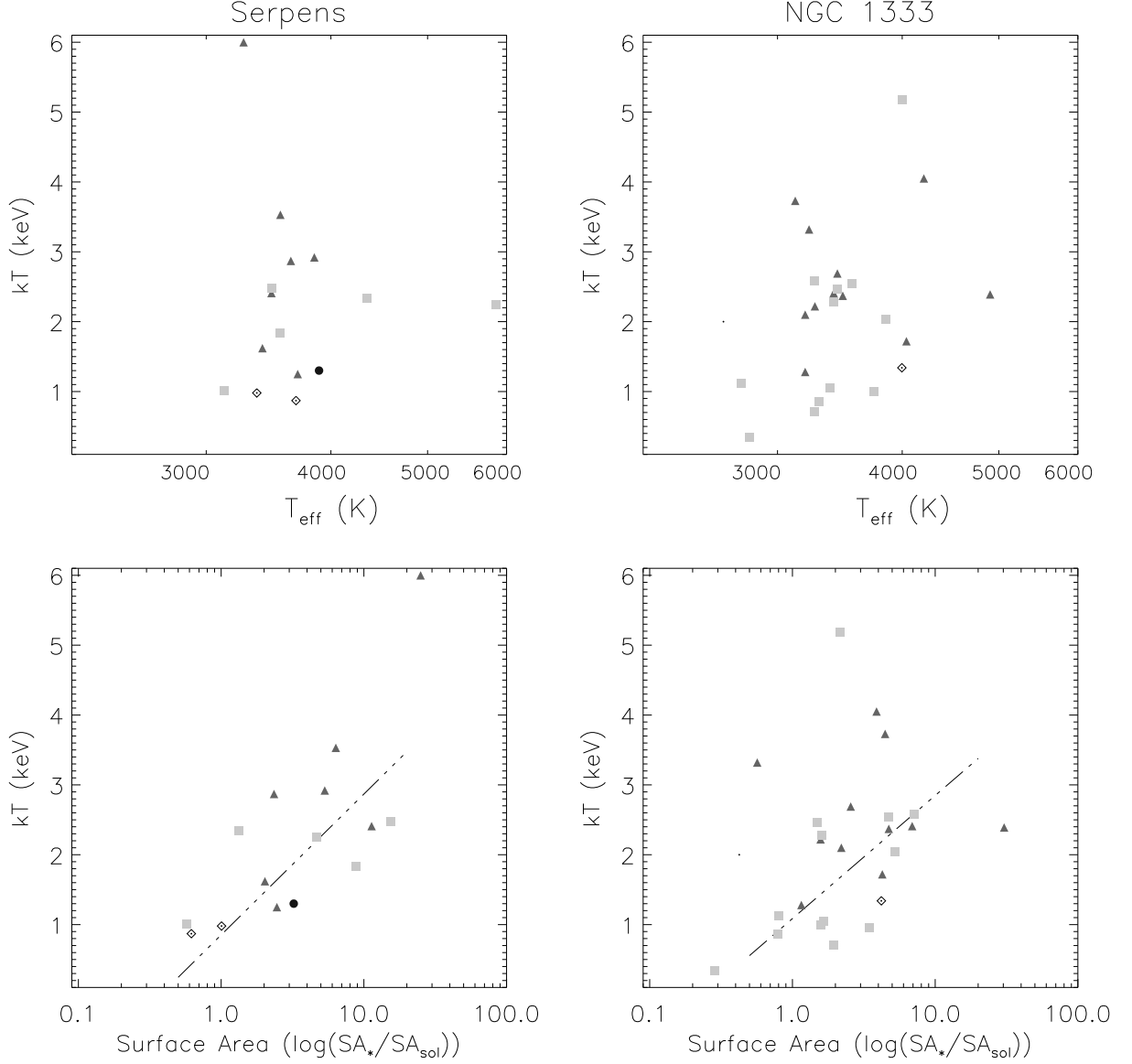


Fig. 12.— The upper plots show T_{eff} against the X-ray plasma temperature, kT . The lower plots show the surface area against kT . A trend of increasing plasma temperature with surface area is noted. Symbols indicate Class 0/I (circle), Flat Spectrum (inverted triangle), Class II (triangle), Transition Disk (diamond), Class III (square). The dash-dot lines show the fits to the data, indicating an increasing trend in kT with surface area, of $kT[\text{keV}] = 0.85 \pm 0.22 + (2.02 \pm 0.28) \log(SA_*/SA_{\text{sol}})$ in Serpens and $kT[\text{keV}] = 1.09 \pm 0.26 + (1.76 \pm 0.22) \log(SA_*/SA_{\text{sol}})$ in NGC 1333. The fits to these plots were made while removing the outlier data points: in Serpens where $kT \approx 6$ keV, and in NGC 1333 where $kT > 3$ keV.

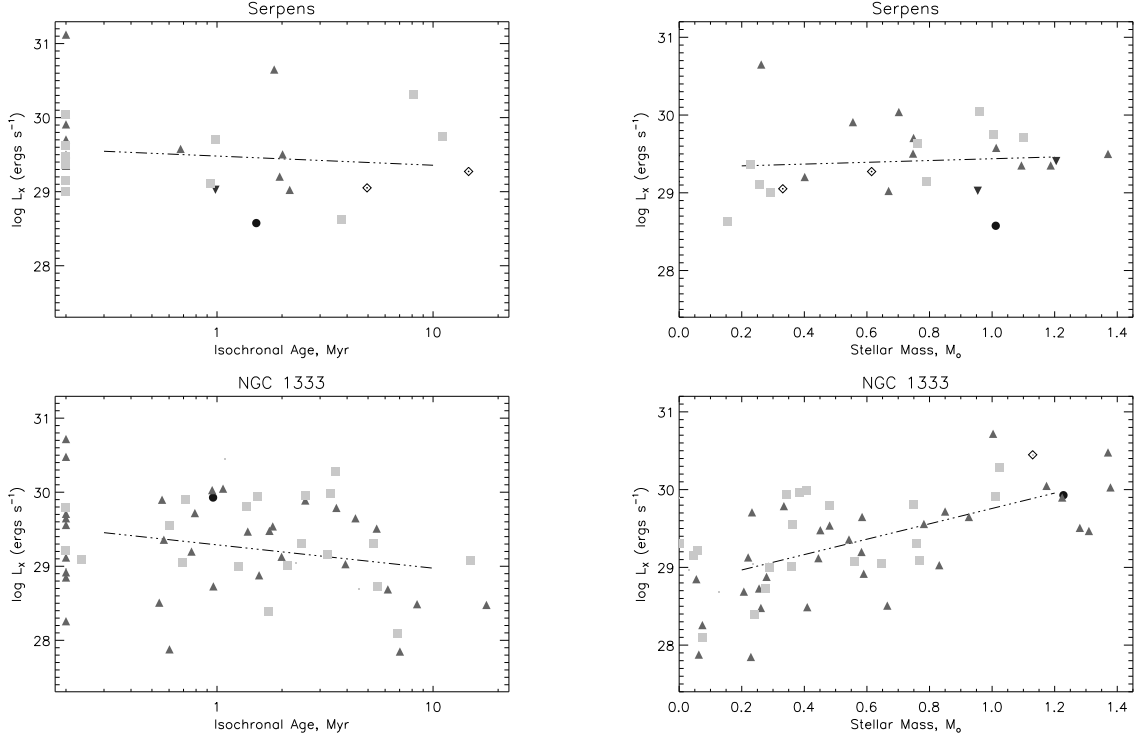


Fig. 13.— The graphs on the left show the stellar isochronal age calculated from Baraffe (1998), plotted against the stellar X-ray luminosity, L_X , for Serpens (above) and NGC 1333 (below). The NGC 1333 data exhibit a marginal trend towards lower luminosities in apparently older stars, the Serpens data do not show a significant trend. The graphs on the right show the stellar mass calculated from Baraffe (1998), M_* , plotted against L_X , for Serpens (above) and NGC 1333 (below). In NGC 1333, there is a weak trend towards increasing X-ray luminosity with increasing stellar mass. Symbols indicate Class 0/I (circle), Flat Spectrum (inverted triangle), Class II (triangle), Transition Disk (diamond), Class III (square). The dot-dashed lines represent the fits to the entire YSO sample of L_X to stellar isochronal age and mass: In NGC 1333 $\log(L_X[\text{ergs}^{-1}]) \propto (-0.32 \pm 0.17) \log(\tau[\text{Myr}])$ and $L_X \propto (0.99 \pm 0.16) \log(M/M_\odot)$, in Serpens $\log(L_X[\text{ergs}^{-1}]) \propto (-0.12 \pm 0.16) \log(\tau[\text{Myr}])$, $(0.12 \pm 0.21) \log(M/M_\odot)$.

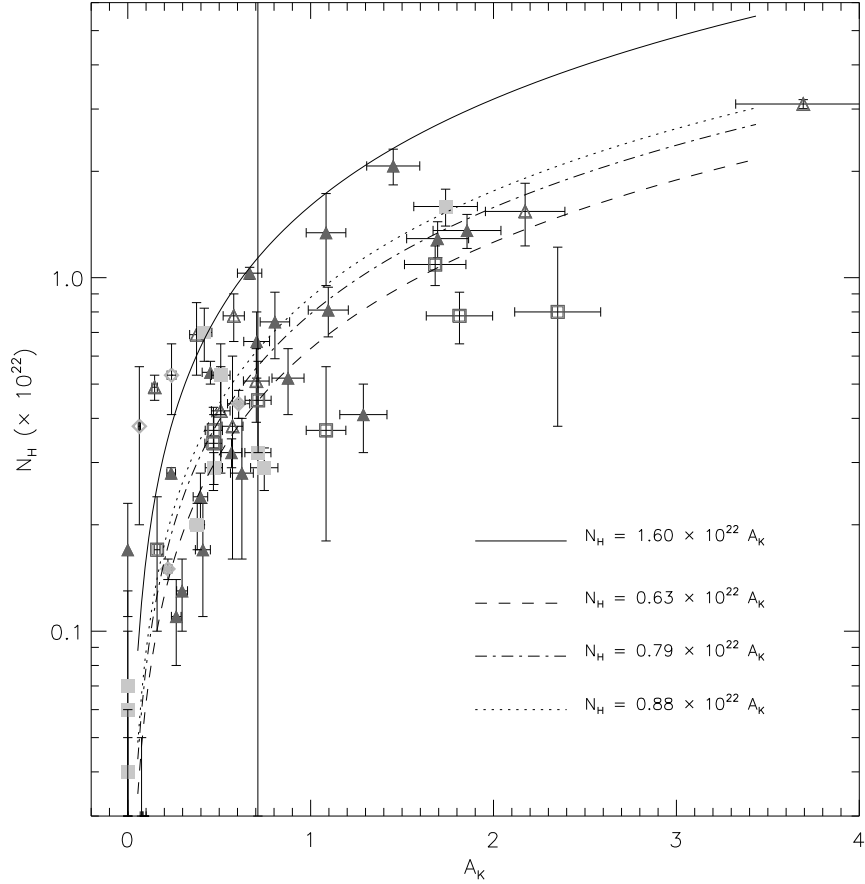


Fig. 14.— The graph plots the N_H v. A_K ratio for the sources from both the Serpens (open symbols) and NGC 1333 (filled symbols) clusters. The squares represent Class III, the triangles Class II, and the diamonds Transition Disk cluster stars. Note that the Class III objects trace only the lower tracks ($N_H = 0.88 \times 10^{22} A_K$ for NGC 1333, $N_H = 0.63 \times 10^{22} A_K$ for Serpens, $N_H = 0.79 \times 10^{22} A_K$ for both clusters), while the Class II objects trace both the lower relation and the standard ISM gas-to-dust ratio of $N_H = 1.6 \times 10^{22} A_K$ (Vuong et al. 2003).